6-2-2020

Monte-Carlo-computed dose, kerma and fluence distributions in heterogeneous slab geometries irradiated by small megavoltage photon fields

Sudhir Kumar

Alan E. Nahum

Indrin J. Chetty
Henry Ford Health System, ICHETTY1@hfhs.org

Recommended Citation
Kumar S, Nahum AE, and Chetty IJ. Monte-Carlo-computed dose, kerma and fluence distributions in heterogeneous slab geometries irradiated by small megavoltage photon fields. Phys Med Biol 2020.

Monte-Carlo-computed dose, kerma and fluence distributions in heterogeneous slab geometries irradiated by small megavoltage photon fields

To cite this article before publication: Sudhir Kumar *et al* 2020 *Phys. Med. Biol.* in press https://doi.org/10.1088/1361-6560/ab98d1

Monte-Carlo-computed dose, kerma and fluence distributions in heterogeneous slab geometries irradiated by small megavoltage photon fields

Sudhir Kumar*[1,2], Alan E Nahum[3] and Indrin J Chetty[1]

[1] Department of Radiation Oncology, Henry Ford Health System, 2799 W. Grand Boulevard, Detroit, MI 48202, USA

[2] Radiological Physics and Advisory Division, Bhabha Atomic Research Centre, CT & CRS building, Anushaktinagar, Mumbai-400094, India

[3]12 Beech House, Ancastle Green, Henley-on-Thames RG9 1UL, UK

***Correspondence:**

Email: **sktomar1@yahoo.co.in**

Abstract

Small-field dosimetry is central to the planning and delivery of radiotherapy to patients with cancer. Small-field dosimetry is beset by complex issues, such as loss of charged-particle equilibrium (CPE), source occlusion and electron scattering effects in low-density tissues. The purpose of the present research was to elucidate the fundamental physics of small fields through the computation of absorbed dose, kerma and fluence distributions in heterogeneous media using the Monte-Carlo method. Absorbed dose and kerma were computed using the DOSRZnrc Monte-Carlo (MC) user-code for beams with square field sizes ranging from 0.25 × 0.25 to 7× 7 cm^2 (for 6 MV 'full linac' geometry) and 0.25 × 0.25 to 16 × 16 cm^2 (for 15 MV 'full linac' geometry). In the bone inhomogeneity the dose *increases* (vs. homogeneous water) for field sizes < 1 × 1 cm^2 at 6 MV and ≤ 3 × 3 cm^2 at 15 MV and *decreases* (vs. homogeneous water) for field sizes ≥ 3 × 3 cm^2 at 6 MV and ≥ 5 × 5 cm^2 at 15 MV. In the lung inhomogeneity there is *negligible decrease* in dose compared to in uniform water for field sizes > 5 × 5 cm^2 at 6 MV and ≥ 16 × 16 cm^2 at 15 MV, consistent with the Fano theorem. The near-unity value of the absorbed-dose to collision-kerma ratio, D/K_{col}, at the centre of the bone and lung slabs in the heterogeneous phantom demonstrated that CPE is achieved in bone for field sizes > 1 × 1 cm^2 at 6 MV and ≥ 5 × 5 cm^2 at 15 MV; CPE is achieved in lung at field sizes > 5 × 5 cm^2 at 6 MV and ≥ 16 × 16 cm^2 at 15 MV. Electron-fluence *perturbation factors* for the 0.25 × 0.25 cm^2 field were 1.231 and 1.403 for bone-to-water and 0.454 and 0.333 for lung-to-water were at 6 and 15 MV respectively. For field sizes large enough for quasi-CPE, the MC-derived *dose*-perturbation factors,

lung-to-water, $\left(DPF\right)_{\mathrm{w}}^{\mathrm{lung}}$ were close to unity; *electron-fluence* perturbation factors, lung-to-water, $\left(p_{\Phi}^{\mathrm{prim}}\right)_{\mathrm{w}}^{\mathrm{lung}}$ were ~1.0, consistent with the 'Fano' theorem. At 15 MV in the lung inhomogeneity the magnitude and also the 'shape' of the *primary* electron-fluence spectrum differed significantly from that in water. Beam penumbrae relative to water were narrower in the bone inhomogeneity and broader in the lung inhomogeneity for all field sizes.

Keywords: absorbed dose, kerma, electron-fluence perturbation, non-equilibrium photon fields, Monte Carlo, Fano theorem.

1. Introduction

Small-field dosimetry is an essential component in the planning and delivery of external-beam radiotherapy. The near-exponential increase in the utilization of hypofractionation, and stereotactic body radiotherapy (SBRT) in particular (e.g. Pan *et al* 2011), where small fields predominate, has cemented small-field dosimetry as an essential foundation of treatment plans designed to meet the goals of high-dose target coverage and sharp gradients to protect surrounding healthy tissues. The accuracy of small-field dosimetry is confounded by several factors, such as loss of charged-particle equilibrium (CPE), source occlusion, the size and type of the detector, and tissue heterogeneity, particularly low-density structures, like lung tissue, where increased electron range and scattering present a formidable challenge. Over the past 10 years there have been many papers and also measurement protocols devoted to addressing the issues associated with small-field dosimetry (Sánchez-Doblado *et al* 2007, Das *et al* 2008, Alfonso *et al* 2008, Scott *et al* 2008, 2009, Bouchard *et al* 2009, IPEM 2010, Francescon *et al* 2011, Scott *et al* 2012, Disher *et al* 2012, Kumar *et al* 2015, Bouchard *et al* 2015, ICRU 2017, IAEA 2017, Benmakhlouf and Andreo 2017).

With regard to dose-perturbation effects in *heterogeneous* media, the literature is also extensive. The following literature review is far from exhaustive. Interested readers are encouraged to consult, for example, Chetty *et al* 2007 and Raynaert *et al* 2007. Jones *et al* (2003) employed the EGS4 Monte-Carlo (MC) system to study the effect of lung (variable densities) on IMRT beamlets using *point-source geometry* linac spectra of 6, 15 and 24 MV photon beams for circular field sizes of diameter ranging from 0.5 – 10 cm. These authors showed that for small fields, the dose decreased drastically in the presence of lung inhomogeneity due to lack of (lateral) electronic equilibrium. Rustgi *et al* (1997) and Rustgi *et al* (1998) performed measurements for cones, 12.5 - 40 mm in diameter, for stereotactic radiosurgery (X-knife, 6 MV photon beam) in low (air) and high

(aluminium) density inhomogeneities respectively and showed that the dose perturbation factor (relative to water) was highly dependent on field diameter and approached unity as the field diameters increased from 12.5 to $\geq$ 25 mm. Small field calculations (< 3 × 3cm^2) were performed for lung-equivalent media using the DPM MC code along with validation measurements. Dose perturbation factors (relative to water) on the central axis within the lung slabs were found to increase at smaller field sizes and higher energies (for 2 × 2 cm^2 values were 0.85 and 0.70 for 6 and 15 MV photon beams, respectively) (Chetty *et al* 2003). Extensive small field calculations and measurements in lung-equivalent and bone-equivalent slab phantoms were also performed to validate calculations from pencil-beam and convolution/superposition algorithms, as well as the PENELOPE MC code for 6 and 18 MV photon beams (Carrasco *et al* 2004, 2007). Significant dose reduction and penumbral broadening was observed, which worsened as the field size was reduced to 1×1 cm^2 in the lung-equivalent phantom. Calculations, and measurements performed to validate the XVMC code in lung and bone slab phantoms showed reductions of ~15% in lung slabs (relative to water) at for 6 MV, 3 × 3 cm^2 photon beams, as well as significant penumbral broadening at the small field sizes (Fragoso *et al* 2010).

Proper management of small fields in treatment planning requires dose algorithms that accurately account for the physics involved. Failure to account for issues such as increased lateral electron scattering in lung tissue by, for example, pencil-beam algorithms employing *radiological pathlength scaling*, can lead to a severe reduction in the dose delivered to the target, potentially reducing the probability of achieving local tumour control (Latifi *et al* 2014, Ohri *et al* 2018). In light of these considerations, we set out to perform detailed Monte-Carlo calculations of dose, kerma and photon/electron fluence distributions in phantoms containing heterogeneous (lung and cortical bone-equivalent) tissues under small (and ultra-small) field conditions. Our in-depth investigation of the perturbation of the fluence distributions by heterogeneous tissues ought to yield a more fundamental understanding of the depth-dose and dose-profile distributions of small-field patient irradiation. The inclusion of photon and electron fluence calculations at 'ultra-small' fields - from 1 × 1 down to 0.25 × 0.25 cm^2 - differentiates our work from that of others, providing knowledge of the physics associated with dose perturbations in heterogeneous tissues; this is of central concern for clinical, small-field treatment planning in regions such as the lung.

2. Materials and methods

2.1. *Monte Carlo modelling of linear accelerator geometry and setting up the simulations*

The EGSnrc Monte-Carlo user-code DOSRZnrc (version: v20019a) was employed to compute dose and kerma. FLURZnrc (version: v20019a) was used to generate photon and electron fluence spectra

(Rogers *et al* 2019). Previously validated Monte-Carlo source models of a Varian 2100C and 2100 iX linear accelerators (Varian Medical Systems, Palo Alto, CA) for 15 and 6 MV photon beams respectively have been employed (Scott *et al* 2008, Underwood *et al* 2013). Phase-space (PS) files from previous studies, e.g. Scott *et al* (2009) and Underwood *et al* (2013), were scored at a distance of 58 cm and 100 cm from the source for 15 and 6 MV MC beam models respectively; these PS files were used as input to the EGSnrc user-codes DOSRZnrc and FLURZnrc using the 'source 21' option (i.e. full beam phase space data, incident on front face) (Rogers *et al* 2019). The transport parameters employed in the EGSnrc simulations are summarized in table 1. The number of histories (up to 6×10^9) in each simulation was such that the average statistical uncertainty was $\leq 0.4\%$. The standard uncertainty propagation method was used to derive the Type A uncertainties (IAEA 2008).

2.2. *Computation of absorbed dose and kerma as a function of depth and field size*

A schematic diagram of the heterogeneous cylindrical slab phantoms for calculation of dose and kerma is displayed in figure 1. The outer radius and height of the cylindrical phantom were 15 and 30 cm, respectively. The *lung-equivalent slab phantom* was composed of 3 cm water/7 cm lung-equivalent material/20 cm water in consecutive arrangement. For the *bone-equivalent slab phantom* the consecutive arrangement was 3 cm water/2 cm bone-equivalent material/25 cm water. Atomic compositions, mass densities (ρ) and mean excitation energies of the materials used to model the heterogeneous cylindrical slab phantoms are listed in table 2. Additionally, a homogeneous phantom (composed entirely of water) having the same physical dimensions as the heterogeneous phantoms was also modelled. The source to phantom surface distance (SSD) was 100 cm.

PEGS4 datafiles were generated for lung (inflated), density 0.21 g cm^{-3}, and cortical bone, density 1.8 g cm^{-3}, using the *ESTAR*[1] program to obtain the density-effect correction to the electronic stopping power. The absorbed dose, D and kerma, K were computed using the DOSRZnrc user-code with *ECUT* (electron/positron total energy cut-off) and *PCUT* (photon energy cut-off) values of 512 keV and 1 keV respectively for photon beams for square field sizes ranging from 0.25×0.25 to 7×7 cm^2 (for 6 MV) and 0.25×0.25 cm^2 to 16×16 cm^2 (for 15 MV) in the heterogeneous cylindrical slab phantoms along the beam central axis (CAX) from the surface to the far end of the cylindrical phantoms using *full linac geometry* PS files generated for these field sizes. Furthermore, the D and K were also computed for the same field sizes and beam qualities in a homogeneous (water) phantom along the CAX at the same depth as computed in the heterogeneous phantoms.

[1] http://physics.nist.gov/PhysRefData/Star/Text/ESTAR.html

A 'point like' cylinder with a circular cross-section of 0.5 mm diameter and (a) 0.5 mm height in the build-up region, interface regions and lung- and bone-like media, (b) 2 mm height elsewhere, centred on the beam central axis, comprised the scoring volume.

2.2.1. *Quantifying the loss of charged particle equilibrium in heterogeneous media: Computation of D/K_{col} as function of field size*

The absorbed-dose to collision-kerma ratio, D/K_{col} is a measure of the degree of CPE or quasi-CPE[2] (IAEA 2017). To quantify this effect, D/K_{col} was computed in the phantoms described in figure 1, for 6 and 15 MV photon beams. The DOSRZnrc (Rogers *et al* 2019) user-code does not score collision kerma K_{col}; we obtained the ratio (K_{col}/K) by computing the 'photon cavity integrals' given below (equations (1) and (2)). Total photon fluence, per MeV per incident particle, down to 1 keV (with above *ECUT*, *PCUT*) was scored on the CAX at depths of 3.975 cm (bone-equivalent medium) and 6.475 cm (lung-equivalent medium) using the FLURZnrc user-code. Parameter option 'SLOTE = -999' where the lowest 90% of the energy range is divided into 'bins' of equal logarithmic widthwith the highest 10% divided into linearly-spaced bins. Kermas K and K_{col}[3] were then calculated over (energy) fluence spectrum using the following cavity integrals (e.g. Nahum 2007):

$$\left[K(z)\right]_{\mathrm{med}} = \int_{PCUT}^{k_{\max}} k\left[\Phi_k^{\mathrm{phot}}\left(\mathrm{z}\right)\right]_{\mathrm{med}} \left(\frac{\mu_{\mathrm{tr}}(k)}{\rho}\right)_{\mathrm{med}} \mathrm{d}k \qquad (1)$$

and

$$\left[K_{\mathrm{col}}(z)\right]_{\mathrm{med}} = \int_{PCUT}^{k_{\max}} k\left[\Phi_k^{\mathrm{phot}}\left(\mathrm{z}\right)\right]_{\mathrm{med}} \left(\frac{\mu_{\mathrm{en}}(k)}{\rho}\right)_{\mathrm{med}} \mathrm{d}k \qquad (2)$$

where k is the photon energy, $\mu_{tr}(k)/\rho$ and $\mu_{en}(k)/\rho$ are the mass energy-transfer coefficient and the mass energy-absorption coefficient respectively, and $\left[\Phi_k^{\mathrm{phot}}\left(\mathrm{z}\right)\right]_{\mathrm{med}}$ is the photon fluence, differential in energy, as a function of depth z in the medium. The quantities $\mu_{tr}(k)/\rho$ and $\mu_{en}(k)/\rho$ have been derived by using the '*g*' user-code of EGSnrc system (Kawrakow *et al* 2019) with the same PEGS4 datafiles as used with DOSRZnrc for computing K. Note that the lower limit of the integral has been

[2]In real photon beams CPE is never 'perfect' due to finite photon attenuation over the distance of the maximum secondary-electron/positron range; we refer to this as quasi-CPE; this corresponds to what Attix (1986) termed 'Transient CPE'.

[3]The present text employs the term 'collision kerma' introduced by Attix (1979a, 1979b), although a recent textbook (Andreo *et al* 2017) prefers *electronic* kerma. ICRU Report 90 (ICRU, 2016) states: 'In the present Report we retain the term collision kerma, although noting that it was presumably named in analogy to the collision stopping power, which was changed to electronic stopping power in ICRU Report 60' (ICRU, 1998).

set equal to *PCUT* since the fluence spectrum only extends down to *PCUT*. From equations (1) and (2),

$$K_{\mathrm{col}}/K = \left(1-\bar{g}\right) \qquad (3)$$

was calculated at depths specified above in the heterogeneous cylindrical phantoms (figure 1) and then multiplied by K computed from DOSRZnrc (same depth and medium) to yield K_{col} as a function of field size. D/K_{col} was derived using the values of D computed at the same depth and medium. D/K_{col} ratios were also derived for thehomogeneous (water) medium at depths of 3.975and 6.475 cm as described in sub-section 2.2. The value of K derived from equation (1) employing the fluence obtained via FLURZnrc agrees within 0.5% with that obtained directly from the results of with user-code DOSRZnrc, for identical normalizations.

Recently Rogers and Townson (2019) created a new user-code, DOSRZnrcKcol, which computes K_{col} directly as a function of position in the phantom. However, DOSRZnrcKcol was not available at the time when this study was carried out. There is no option in DOSRZnrcKcol to model a *heterogeneous* cylindrical phantom (Rogers and Townson 2019). Here user-code DOSRZnrc has been employed (v2019a) for computing K_{col} in heterogeneous as well as homogeneous phantoms for consistency. Therefore, the same approach was used as adopted previously by Kumar *et al* (2015a).

2.2.1.1. *Determination of* $\bar{g}$ *as function of field size*

In equation (3), the quantity $\bar{g}$ is the average value of the fraction of the initial kinetic energy of the secondary electrons that is re-irradiated as bremsstrahlung. It depends on energy of electrons, E and atomic number, Z of the material. In order to evaluate the variation of $\bar{g}$ within the different materials and at different energies, $\bar{g}$ was computed from equation (3) for the same geometries specified in sub-section 2.2.

2.2.2. *Computation of MC-derivedinhomogeneity dose perturbation factoras a function of depth and field size*

The inhomogeneity dose perturbation factor, *DPF* is defined as the Monte-Carlo derived ratio of the dose in the heterogeneous phantom, $D(z)_{\mathrm{hetero}}$ at a depth, z, to the dose in the homogeneous (water) phantom, $D(z)_{\mathrm{w}}$ at the same physical depth, z and for the same set-up conditions (e.g. Li *et al* 2000, Jones *et al* 2003):

Dose, kerma and fluence distributions in heterogeneous slab geometries under non-equilibrium conditions

$$\left[DPF(z)\right]_{\mathrm{w}}^{\mathrm{hetero}} = \frac{D(z)_{\mathrm{hetero}}}{D(z)_{\mathrm{w}}} \qquad (4)$$

where 'hetero' and 'w' indicate the heterogeneous (water-bone/lung-water) and homogeneous water phantoms, respectively. From equation (4), $\left[DPF(z)\right]_{\mathrm{w}}^{\mathrm{hetero}}$, will be referred to as the '*MC-derived dose-perturbation factor hetero-to-water'*. $\left[DPF(z)\right]_{\mathrm{w}}^{\mathrm{bone}}$ and $\left[DPF(z)\right]_{\mathrm{w}}^{\mathrm{lung}}$ were computed at depths of 3.975 and 6.475 cm depth in the bone-equivalent and lung-equivalent slab phantoms respectively, for the 6, 15 MV photon beams and the range of field sizes described earlier.

2.3. *Primary electron (+positron) fluence spectra in heterogeneous media and water and the computation of* $\left(p_{\Phi}^{\mathrm{prim}}\right)_{\mathrm{w}}^{\mathrm{hetero}}$

The primary electron (+positron) fluence spectra down to 1 keV (kinetic energy), per MeV per unit incident particle, have been computed using FLURZnrc. By *primary* is meant all charged particles (electrons, positrons) that are not 'delta rays' (aka 'knock-on electrons'); this also applies to charged particles liberated by *secondary* bremsstrahlung. The scoring geometry for the fluence spectra is shown in figure 1.

We define the *primary electron fluence perturbation factor*, $\left(p_{\Phi}^{\mathrm{prim}}\right)_{\mathrm{w}}^{\mathrm{hetero}}$ as

$$\left(p_{\Phi}^{\mathrm{prim}}\right)_{\mathrm{w}}^{\mathrm{hetero}} = \frac{\left[\Phi^{\mathrm{prim}}(z)\right]_{\mathrm{hetero}}}{\left[\Phi^{\mathrm{prim}}(z)\right]_{\mathrm{w}}} = \frac{\int_0^{E_{\max}} \left[\Phi_E^{\mathrm{prim}}(z)\right]_{\mathrm{hetero}} \mathrm{d}E}{\int_0^{E_{\max}} \left[\Phi_E^{\mathrm{prim}}(z)\right]_{\mathrm{w}} \mathrm{d}E} \qquad (5)$$

where $\left[\Phi_E^{\mathrm{prim}}(z)\right]_{\mathrm{hetero}}$ and $\left[\Phi_{\mathrm{E}}^{\mathrm{prim}}(z)\right]_{\mathrm{w}}$ are the *primary* electron (+ positron) fluences, differential in energy, (i.e. excluding delta-rays), at depth 'z' in the heterogeneous media (bone, lung) and homogeneous medium (water), respectively. Note that $\left(p_{\Phi}^{\mathrm{prim}}\right)_{\mathrm{w}}^{\mathrm{hetero}}$ depends on the field size FS, beam quality Q and depth 'z' as well as on the medium. The *primary electron fluence perturbation factors* bone-to-water, $\left(p_{\Phi}^{\mathrm{prim}}\right)_{\mathrm{w}}^{\mathrm{bone}}$, and lung-to-water, $\left(p_{\Phi}^{\mathrm{prim}}\right)_{\mathrm{w}}^{\mathrm{lung}}$, were computed from equation (5) at depths of 3.975 and 6.475 cm depth in the bone-equivalent and lung-equivalent slab phantoms respectively for 6, 15 MV photons and the range of field sizes described earlier.

2.4. *Comparison of the MC-derived dose perturbation factor, hetero-to-water, to* $\left(p_{\Phi}^{\text{prim}}\right)_{\text{w}}^{\text{hetero}}$ *ratio with the Bragg-Gray stopping-power ratio* $s_{\text{med,w}}^{\text{BG}}$

The absorbed dose to medium, $D(z)_{\text{med}}$, at a specified depth, z, is related to the absorbed dose to water, $D(z)_{\text{w}}$, by

$$D(z)_{\text{med}} = D(z)_{\text{w}} \times s_{\text{med,w}}^{\text{BG}} \times \left(p_{\Phi}^{\text{prim}}\right)_{\text{w}}^{\text{med}} \tag{6}$$

where $s_{\text{med,w}}^{\text{BG}}$ is the Bragg-Gray, or unrestricted (electronic) stopping-power ratio[4], medium-to-water, involving the *primary* electron (+ positron) fluence (Nahum 1978, Nahum 2007, Andreo *et al* 2017). The perturbation factor defined in terms of the *primary* electron fluence (equation (5)), is consistent with this. For bone and lung media this becomes:

$$\frac{D(z)_{\text{bone}}}{D(z)_{\text{w}}} = s_{\text{bone,w}}^{\text{BG}} \times \left(p_{\Phi}^{\text{prim}}\right)_{\text{w}}^{\text{bone}} \tag{7}$$

and

$$\frac{D(z)_{\text{lung}}}{D(z)_{\text{w}}} = s_{\text{lung,w}}^{\text{BG}} \times \left(p_{\Phi}^{\text{prim}}\right)_{\text{w}}^{\text{lung}} \tag{8}$$

Using equation (4), equations (7) and (8) can be written:

$$\frac{\left[DPF(z)\right]_{\text{w}}^{\text{bone}}}{\left(p_{\Phi}^{\text{prim}}\right)_{\text{w}}^{\text{bone}}} \simeq s_{\text{bone,w}}^{\text{BG}} \tag{9}$$

and

$$\frac{\left[DPF(z)\right]_{\text{w}}^{\text{lung}}}{\left(p_{\Phi}^{\text{prim}}\right)_{\text{w}}^{\text{lung}}} \simeq s_{\text{lung,w}}^{\text{BG}} \tag{10}$$

Implicit in the above expressions is the assumption that though the electron fluences in bone and lung and in water may differ in magnitude, the *energy spectra* have similar shapes. This assumption is investigated explicitly in this work.

[4]The Bragg-Gray stopping-power ratio is employed as, to a good approximation; there will be delta-ray equilibrium in all three extended media (Andreo *et al* 2017).

In order to evaluate this approximation to the unrestricted (electronic) stopping-power ratio, bone-to-water, $s^{\mathrm{BG}}_{\mathrm{bone,w}}$, and lung-to-water, $s^{\mathrm{BG}}_{\mathrm{lung,w}}$ as computed from equations (9) and (10), were compared with the same quantities obtained from the *ESTAR* database[5]. Note that fluence-weighted mean energy, $\overline{E}$, was determined from the 'primary' electron (+ positron) fluence spectra generated by FLURZnrc; the *unrestricted* mass electronic stopping powers $\left\{S_{\mathrm{el}}(\overline{E})/\rho\right\}$ corresponding to $\overline{E}$ for each of the materials, bone, lung and water were then determined from *ESTAR*, and used to compute the appropriate ratios. We will denote the ratios $s^{\mathrm{BG}}_{\mathrm{bone,w}}$ and $s^{\mathrm{BG}}_{\mathrm{lung,w}}$ derived from *ESTAR* (*conventional* method) as $\left(s^{\mathrm{BG}}_{\mathrm{bone,w}}\right)_{\mathrm{cav\,th}}$ and $\left(s^{\mathrm{BG}}_{\mathrm{lung,w}}\right)_{\mathrm{cav\,th}}$ respectively to distinguish them from the pseudo - $s^{\mathrm{BG}}_{\mathrm{bone,w}}$ and $s^{\mathrm{BG}}_{\mathrm{lung,w}}$ computed using equations (9) and (10).

2.5. *Mean electron energy*

Mean electron (+ positron) energies were obtained from:

$$\overline{E}(z)=\frac{\int_0^{E_{\max}} E\,\Phi_{\mathrm{E}}^{\mathrm{tot}}(z)\,\mathrm{d}E}{\int_0^{E_{\max}} \Phi_{\mathrm{E}}^{\mathrm{tot}}(z)\,\mathrm{d}E} \qquad (11)$$

where $\Phi_{\mathrm{E}}^{\mathrm{tot}}(z)$ is the *total* electron (+ positron) fluence, differential in energy (i.e. including all generations of 'knock-on' electrons, or delta-rays) at different depths *z*. The total electron (+positron) fluence spectra per MeV per unit incident particle down to 1 keV were generated using the FLURZnrc user-code, with the same *ECUT* and *PCUT* and geometries as above (sub-sections 2.2, 2.2.1).

2.6. *Computation of total photon fluence, differential in energy*

The total photon fluence per MeV per incident particle down to 1 keV was generated using the FLURZnrc user-code, with the same parameter settings and geometries as above (sub-sections 2.2, 2.2.1). From the photon fluence, differential in energy, $\left[\Phi_k^{\mathrm{phot}}(\mathrm{z})\right]_{\mathrm{med}}$, the photon-fluence-weighted mean energy, $\overline{E}_k$, was derived as a function of field size, using equation (11).

2.7. *Generation of transverse (cross-plane) and determination of penumbra*

[5] http://physics.nist.gov/PhysRefData/Star/Text/ESTAR.html

Dose, kerma and fluence distributions in heterogeneous slab geometries under non-equilibrium conditions

Absorbed dose (in the left-right direction) was computed using the DOSRZnrc user-code with *ECUT* and *PCUT* described above (sub-section 2.2) for a 6 MV photon beam at the depth of 4 cm (3-5 cm depth, bone slab) and 7 cm depth (3-10 cm depth, lung slab) with square field sides ranging from 0.25 to 5 cm defined at 100 cm SSD (figure 1). Dose was also computed in the water phantom. For all comparisons, dose per incident fluence was normalized to that at depth of maximum dose (d_{max}) along the CAX for a 10 × 10 cm^2 field in the water phantom. This point represents the absolute dose calibration point of the linear accelerator where the condition 1 cGy/MU applies. The transverse profiles were plotted for heterogeneous media (bone, lung) and compared with the profiles in water generated in the same plane. To compute the beam penumbra, doses were normalized to their respective maximum dose values along the beam CAX. Penumbra was defined as the distance between the 80%-20% relative doses at the defined depth and field size in the given medium (IPEM 2010).

3. Results and Discussion

3.1. *Computation of absorbed dose and kerma as a function of depth and field size*

Figures 2(a)-(d) show the absorbed dose computed in the heterogeneous cylindrical phantoms (bone-equivalent and lung-equivalent slab phantoms) along the beam CAX for the 6 and 15 MV photon beams. In figures 2(a)-(b), dose 'build-up' and 'build-down' are observed at the proximal and distal ends of the bone inhomogeneity, respectively. Dose 'build-up' ($\leq 0.75 \times 0.75$ cm^2 at 6 MV and $\leq 1 \times 1$ at 15 MV) at the proximal end of the bone inhomogeneity is due partly to increased backscattering of the secondary electrons from bone which has a higher atomic number ($Z_{eff} = 13.8$) and high density ($\rho = 1.8$ g cm^{-3}) than water ($Z_{eff} = 7.42$, $\rho = 0.998$ g cm^{-3}) (Das and Khan (1989)). Dose enhancement at proximal end of the bone inhomogeneity (figures 2(a)-(b)) is also demonstrated by figure 3 where the total electron (+positron) fluences, differential in energy, in the bone-equivalent slab phantom is significantly higher than that in the homogeneous (water) phantom at same depth (dashed curve). This effect is accentuated in the low energy region, demonstrating that low energy electron (+positron) fluence is increased near the water-bone interface (proximal end) due to the presence of bone. Dose 'build-down' at distal end of the bone inhomogeneity is partly attributable to decreased backscattering of the secondary electron from the water and can be described similarly. The (lateral) electronic disequilibrium at the interfaces is more prominent at15 MV relative to 6 MV because of greater range of the lateral electrons.

The absorbed dose is enhanced in the bone inhomogeneity region (vs. homogeneous water) for field sizes $< 1 \times 1$ cm^2 at 6 MV, and $\leq 3 \times 3$ cm^2 at 15 MV (figures 2(a)-(b)). The magnitude of dose enhancement decreases as the field size increases. For instance, at 0.25 × 0.25 cm^2 dose enhancements were 10.8% and 28.7% at 6, and 15 MV respectively. This is likely because the range

of electrons in bone is smaller than that in water resulting in slower loss of CPE in bone versus water as field size is reduced. Moreover, at these ultra-small field sizes (1×1 cm^2) the contribution to dose on the CAX is primarily from electrons travelling in the forward direction implying that these electrons are more energetic. As the field size increases, more electrons scattering at wider angles (or lower energy) contribute to the dose on the CAX, which reduces the mean energy. Note from table 7, the mean electron energies in the 6 MV photon beam at 3.975 cm depth in bone on the central axis for field sizes of 0.25×0.25 and 3×3 cm^2 are 1.047 and 0.963 MeV, respectively, which represents an increase of 8.7% in the mean electron energy at the 0.25 cm field size.When quasi-CPE is established, at field sizes $> 1 \times 1$ cm^2 (6 MV) and $> 3 \times 3$ cm^2 (15 MV) in the bone-equivalent slab phantom, density differences play a negligible role and the dose variationin the bone region (at both proximal and distal interfaces) relative to the water phantom, is significantly reduced. This is clearly visible for field sizes, 3×3 cm^2 at 6 MV and 5×5 cm^2 at 15 MV. Dose reduction in the bone region relative to water under quasi-CPE is understood by elaboration of the interaction cross sections. Compton interaction cross section per unit mass, σ/ρ, (or the mass attenuation coefficient) depends upon the number of electrons per gram of the material (Andreo *et al* (2017)). The number of electrons per gram (e/g) for bone is 3.0×10^{23} which is 10.2% lower than that for water ($= 3.34 \times 10^{23}$).

In figures 2(c)-(d), dose 'build-down' occurs at the proximal, water/lung interface while dose 'build-up' occurs at the distal, lung/water interface. Dose 'build-down' is partly attributed to decreased backscattering of the secondary electrons from the lung material, while the dose 'build-up' at the distal end interface is partly due to increased backscattering of the secondary electrons from water, which has higher mass density (ρ = 0.998 g cm^{-3}) relative to lung (ρ = 0.21 g cm^{-3}). When electrons enter the lung region, they undergo significant lateral scattering in the low-density lung region carrying energy away from the CAX, resulting in a large reduction in dose in the lung region. The dose reduction increases as the field sizes decrease to 0.25×0.25 cm^2 since the loss of CPE becomes more significant. For instance, the mean electron (+positron) energy for the 0.25×0.25 cm^2 field is 1.155 MeV (6 MV photon beam), corresponding to R_{csda} values of 2.483 cm (in lung) and 0.521 cm (in water) demonstrating the significant increase in the range of electrons in the lung relative to water. Media density can significantly perturb dose distributions when the field width is small and moreover dose to media depends critically on its densities (Alison *et al* 2012, Fenwick *et al* 2013, Underwood *et al* 2013b, Kumar *et al* 2015). Dose reduction in the lung region is greater at 15 MV where the lateral electronic disequilibrium is further amplified because of the greater electron range compared to 6 MV.

Beyond the distal end of the lung inhomogeneity, dose increases and is higher than the dose relative to that in the homogeneous (water) phantom. This is a consequence of the reduction in attenuation of photons in the lung relative to water. As the field size increases, the dose reduction in lung region becomes less pronounced. At field size broad enough ($> 5 \times 5$ cm^2 for 6 MV, $\geq 16 \times 16$

cm^2 for quasi-CPE, the role of the mass density differences between lung and water media becomes negligible and the dose deficit in the lung virtually disappears. This is consistent with the 'Fano' theorem (Fano 1954, Andreo *et al* 2017): 'In an infinite medium of given atomic composition exposed to a uniform fluence of uncharged particles, the fluence of secondary radiation is also uniform and independent of the density of the medium, as well as of density variations from point to point'. The atomic number differences between water (Z_{eff} = 7.42) and lung (Z_{eff} = 7.77) are negligible and hence any differences between their respective mass interaction coefficients (mass-energy absorption coefficient and electronic stopping power) will also be negligible. Therefore, the considerable density difference between lung (ρ = 0.21 g cm^{-3}) and water (ρ = 0.998 g cm^{-3}) becomes immaterial once the field size is broad enough to establish quasi-CPE; the Fano theorem ensures identical (secondary) electron fluences in the two materials. The results for the lung phantom are consistent with those of previous studies (Chetty *et al* 2003, Rice *et al* 1988).

3.1.1. *Quantifying the loss of charged particle equilibrium in heterogeneous media: D/K_{col} as function of field size*

Figures 4(a)-(b) show the field-size dependence of D/K_{col} along the central axis at a depth of 3.975 cm in the cylindrical bone-equivalent and homogenous (water) phantoms for 6 and 15 MV photons. Figures 4(c)-(d) shows D/K_{col} ratios for lung-equivalent and water phantoms at 6.475 cm depth. In figures 4(a)-(b) it is seen that D/K_{col} decreases rapidly as the field size decreases below 1×1 cm^2 at 6 MV in bone, and below 3 × 3 cm^2 at 15 MV in bone. Field sizes > 1 × 1 cm^2 (figure 4(a)) and ≥ 5 × 5 cm^2 (figure 4(b)) are adequate for achieving the lateral electronic equilibrium for 6 and 15 MV photon beams respectively in bone. Figure 4(a) also shows that lateral electronic equilibrium in the homogeneous (water) phantom is achieved for a field size of ≥ 2 × 2 cm^2 for 6 MV photons, consistent with the study by Bjärngard *et al* (1990).

For the lung-equivalent phantom, figures 4(c)-(d) show that D/K_{col} decreases rapidly as the field size is reduced below 5 × 5 cm^2 and 16 × 16 cm^2, for 6 and 15 MV photons, respectively. This is a consequence of the onset of (lateral) electronic *dis*equilibrium when the field width becomes too small to encompass the increased lateral excursions of electrons in the lung medium (Chetty *et al* 2003, Scott *et al* 2009, IPEM 2010, Kumar *et al* 2015a). Also noted from the D/K_{col} plots is that lateral electronic disequilibrium within lung-equivalent media can be mitigated at field sizes > 5 × 5 cm^2 (6 MV), and ≥ 16 × 16 cm^2 (15 MV). Our results are also consistent with that of Mackie *et al* (1985) who suggested that field sizes < 5 × 5 cm^2 were inadequate for achieving lateral electronic equilibrium in lung tissues irradiated by 15 MV photon beams.

The geometric effect of source occlusion resulting from the finite source width of electrons striking the target in a photon beam linear accelerator is another contributing factor to dose reduction at small field sizes (Das *at al* 2008, IPEM 2010, Kumar *et al* 2015). Kumar *et al* (2015) demonstrated

that the source occlusion effect was significant below field sizes of approximately 0.75 × 0.75 cm^2. This implies that at field sizes < 0.75 × 0.75 cm^2 geometric source occlusion contributes to reduction of dose in addition to that resulting from loss of CPE due to the electron range, producing substantial reduction of dose at these ultra-small field sizes. Considering the ratio: D/K_{col}, it should be noted that D, which incorporates effects of both loss of CPE and source occlusion falls faster than K_{col}, which includes source occlusion only (Kumar *et al* 2015).

3.1.1.1. *Determination of* $\bar{g}$ *as function of field size*

Tables 3 presents the $\bar{g}$ values for bone, lung and water media versus field size for the 6 and 15 MV photon beams. The $\bar{g}$ value decreases as the field size increases. This can be understood by reference to figure 5[6] which shows that the ratio of low-energy photon fluence (< ~0.5 MeV) to the primary fluence increases from the smallest (0.25 × 0.25 cm^2) to largest field size (5 × 5 cm^2) because of the increased fraction of scattered photons as the field sizes increases. Consequently, the mean secondary electron energy decreases with increasing field size resulting in reduced bremsstrahlung production and smaller $\bar{g}$ value as the field size increases, considering that the cross section for bremsstrahlung production varies as EZ^2. Note also that the $\bar{g}$ values are significantly higher for bone relative to lung due to the much higher effective atomic number of bone at MV energy ranges.

3.1.2. *Computation of MC-derived inhomogeneity dose perturbation factor as a function of depth and field size*

Figures 6(a)-(d) show the MC-derived dose perturbation factors, *DPF*s, computed from equation (4) in the heterogeneous cylindrical phantoms for 6 and 15 MVphotons as a function of field size.

The *DPF*s plotted in figures 6(a)-(b) follow the same trend as the depth-dose curves in the bone-equivalent phantom in figures 2(a)-(b). The *DPF* at a given distance from proximal end of the bone inhomogeneity decreases as the field size increases; it is greater than unity for the sub-equilibrium field sizes, and less than unity for the field sizes where quasi-CPE is established. In the bone region, the *DPF* at a given distance from the proximal end of the bone inhomogeneity increases as the photon beam energy increases. These effects are discussed at length in sub-section 3.1. In table 7 it can be noted that the mean electron energies in the 15 MV photon beam at 3.975 cm depth in bone on the CAX for field sizes of 0.25 × 0.25 cm^2 and 3 × 3 cm^2 are 2.506 and 2.048 MeV respectively, represents an increase of 22.4% from the larger to the smaller field size; the corresponding increase in mean electron energy for 6 MV is only 8.7%.

[6]As an explanation, we have shown the amount of low-energy photon fluence relative to the primary fluence for the bone medium for 15 MV photon beams. The pattern will be similar for other media and photon energies.

At 6 MV, the dose perturbation factor, water-to-bone, $\left[DPF(z)\right]^{\mathrm{w}}_{\mathrm{bone}}$ i.e. the MC-derived ratio of dose-to-water to dose-to-bone at 3.975 cm depth in the bone-equivalent slab phantom (figure 1) for a field size (3×3 cm^2) large enough for quasi-CPE, is equal to 1.058 ± 0.007 which is consistent with that predicted by 'large photon cavity' theory: $\left(\overline{\mu}_{\mathrm{en}}/\rho\right)^{\mathrm{w}}_{\mathrm{bone}} = 1.066$. This result is also consistent with Reynaert *et al* (2018) who found a water-to-bone dose ratio of the order of 1.06 for 6 MV photons from a Cyberknife™ beam.

The behaviour of the *DPF* in the lung slab (figures 6(c)-(d)) is entirely consistent with that of the depth-dose curves in figures 2(c)-(d). The *DPF* at a given distance from proximal end of the lung inhomogeneity decreases as the field size decreases. At field sizes wide enough for quasi-CPE, the *DPF* is ≥ 1.0; the slight increase is due to lower photon attenuation in lung. These effects are reviewed in detail in sub-section 3.1.

3.2. *Primary electron (+positron) fluence spectra in heterogeneous media and water and the computation of* $\left(p^{\mathrm{prim}}_{\Phi}\right)^{\mathrm{hetero}}_{\mathrm{w}}$

Figures 7(a) (6 MV, bone inhomogeneity), 7(b), (c) (15 MV, bone inhomogeneity) and 7(d) (15 MV, lung inhomogeneity) demonstrate the 'perturbation' of the (primary) electron fluence spectrum in small, non-equilibrium photon fields.The dotted curves in figures 7(a)-(c) (corresponding to the water medium) lie well below the full curves (bone). Similarly, the dotted curve in figure 7(d) (corresponding to lung medium) lies significantly below the full curve (water). The dashed curves were obtained by multiplying these dotted curves by the bone-to-water (figures 7(a)–(c)) and water-to-lung (figure 7(d)) perturbation factors, defined by equation (5). From figure 7(a) where $\left(p^{\mathrm{prim}}_{\Phi}\right)^{\mathrm{bone}}_{\mathrm{w}} = 1.231$, for 6 MV ($0.25 \times 0.25$ cm^2), the 'corrected' water fluence is almost identical to the 'bone' fluence at all energies implying that there is a negligible change in the spectral 'shape'. At 15 MV (0.25×0.25 cm^2, figure 7(b)), where $\left(p^{\mathrm{prim}}_{\Phi}\right)^{\mathrm{bone}}_{\mathrm{w}} = 1.403$, a significant difference is observed between the 'bone' fluence and the corrected 'water' fluence, which is greatest at low energies, suggesting that the bone medium perturbs not only the magnitude but also the shape of the *primary* electron (+positron) fluence spectrum. As the field size increases the shape of the *corrected* primary electron (+positron) fluence spectrum is preserved (see figure7(c), 15 MV, 2×2 cm^2).

In figure 7(d), for 15 MV, 0.25×0.25 cm^2, where $\left(p^{\mathrm{prim}}_{\Phi}\right)^{\mathrm{lung}}_{\mathrm{w}} = 0.333$, a clear difference between the 'water' and corrected 'lung' media spectra is observed, especially at intermediate energies, implying that the lung medium perturbs both the magnitude *and* the shape of the *primary*

electron (+positron) fluence spectrum; this is due to increased electron lateral scattering in lung and consequent loss of (lateral) electronic equilibrium.

Table 4 presents the MC-derived *primary* electron fluence perturbation factors, $\left(p_{\Phi}^{\text{prim}}\right)_{\text{w}}^{\text{bone}}$, and $\left(p_{\Phi}^{\text{prim}}\right)_{\text{w}}^{\text{lung}}$, as a function of field size for the 6 and 15 MV beams. The bone-to-water perturbation factors are >1.0 for all field sizes due to the hardening effect of bone on the electron spectra. These perturbation factors also increase at the smallest field sizes. The lung-to-water perturbation factors are <1.0 for small photon fields because CPE is lost and therefore the 'Fano' theorem cannot be invoked (Harder 1974). The perturbation factors approach unity as the field size increases. These effects have been described at length in sub-section 3.1.

3.3. *Comparison of the MC-derived dose perturbation factor, hetero-to-water, to* $\left(p_{\Phi}^{\text{prim}}\right)_{\text{w}}^{\text{hetero}}$ *ratio with the Bragg-Gray stopping-power ratio* $\left(s_{\text{med,w}}^{\text{BG}}\right)_{\text{cav th}}$

Table 5 compares the approximate stopping power ratios for the bone and lung heterogeneities to water computed using equations (9) and (10), with those determined from the *ESTAR* database. For 6 MV in bone, the agreement was much less than 1.0% across all field sizes; for 15 MV in bone, agreement on the order of 1.0% was noted with maximum discrepancy of ~1.5% for the 0.25 × 0.25 cm^2 field. In the lung phantom, at 6 MV, differences for field sizes > 0.5 × 0.5 cm^2 were ≤ 1.0% but increased to ~2.5% for the 0.5 × 0.5 cm^2 field. Differences for 15 MV in lung were generally larger ranging from 2-3% for field sizes ≥ 3 × 3 cm^2 to 5.5% at 0.25 × 0.25 cm^2. These discrepancies are likely dueto the change/distortionof the spectral shape between lung and homogeneous water, and breakdown of the approximation at ultra-small field sizes as illustrated in figure 7(d).Table 6 gives a comparison of the $s_{\text{bone,w}}^{\text{BG}}$ and $s_{\text{lung,w}}^{\text{BG}}$ determined using equations (9) and (10) respectively with those derived by Siebers *et al* (2000), for 6 MV and 15 MV photons at 10 × 10 cm^2. These authors employed a different Monte-Carlo code (MCNP), and linear accelerator energy spectra (Mohan *et al* 1985). Our results are on average within 0.8% of their values.

3.4. *Spectra mean energy for electron and photon fluence*

Figures 8(a)-(b) show the variation of the mean electron (+ positron) energies in the heterogeneous bone-equivalent and lung-equivalent slab phantoms, respectively for 6 MV photons. The mean energy was evaluated from equation (11). It is seen from these figures that the mean electron energy for each field size increases gradually as depth increases. This can be understood by the reference to figure 9 which shows for a 0.25 × 0.25 cm^2 field size that the mean photon energy increases with depth in the bone phantom due to beam hardening. A further observation from figures 8(a)–(b) is that there is a

modest increase in electron (+positron) mean energies at all field sizes from the surface to the depth where (quasi) CPE is first established as Andreo and Nahum (1985) first pointed out. In bone and lung phantoms (figures 8(a)-(b)) the mean electron energy increases as the field size is reduced because of the increased fraction of forward scattered, and hence higher energy electrons, contributing to dose on the beam CAX, relative to larger field sizes, as explained previously. For the lung phantom (figure 8(b)), the mean electron energy stays relatively constant in the lung slab due to the increased electron scattering in the lung, and hence beam 'softening' of the electron energy spectrum.

Tables 7and 8 present the spectra mean energy of photon and electron fluence, and R_{csda} values at depths of 3.975 cm depth (bone inhomogeneity) and 6.475 cm depth (lung inhomogeneity) for the 6 and 15 MV photon beams. The photon mean energy, $\overline{E}_k$ was evaluated from photon fluence spectra, differential in energy from equation (11) by replacing $\Phi_{\mathrm{E}}^{\mathrm{tot}}(z)$ by $\Phi_k^{\mathrm{phot}}(\mathrm{z})$. There are several factors driving the observed trends: (a) attenuation differences resulting from different mass densities between bone, lung and water; (b) electron scattering differences between bone, lung and water and loss of CPE at small field sizes; (c) source occlusion effects at ultra-small field sizes; (d) increased phantom scattering. The variation of the mean photon energy with field size in the bone phantom is much larger than that in the lung phantom. This is because of the increased attenuation and beam hardening observed in the bone phantom relative to lung. The bone acts as a better filter of low energy photons compared to lung (see figure 5). On the other hand, the variation of the mean electron energy with field size in the bone phantom is much smaller than that in the lung phantom. This is because there is gradual hardening of the electron spectrum in the bone phantom at all depths (for all field sizes) implying a gradual change in the electron spectrum (see figure 8(a)). However, in the lung phantom there is a 'softening' of the electron spectrum due to increased electron scattering and reduced attenuation in the lung slab (see figure 8(b)); these scattered electrons within the lung slab contribute to a greater degree to the mean electron energy variation with field size versus the bone phantom. The source occlusion effect observed at field sizes $\leq 0.75 \times 0.75$ cm^2 causes reduced photon fluence but also leads to preferential selection of photons scattered in the forward direction, which have higher energy, analogous to a 'pencil beam'. This likely explains the increase in the mean photon and electron energies, and R_{csda} ranges at the smallest field sizes.

3.5. *Generation of transverse* (*cross-plane*) *and determination ofpenumbra*

Figures 10(a)-(d) show the cross-plane dose profiles at depths of 4 and 7 cm depth in the bone and the lung-equivalent slab phantoms, respectively for 6 MV photons. Profiles in the homogenous (water) phantom at the same depths are shown in the plots for comparison. All profiles were normalized to absorbed dose per incident fluence computed at d_{max} along the CAX for a 10×10 cm^2 field size in a homogeneous (water) phantom. In figure 10(a) the 0.5×0.5 cm^2 field profile in bone is slightly

sharper than that in water, likely due to the reduced electron range in bone relative to water. A similar effect is observed for the 3 × 3 cm^2 profiles (figure 10(b)), where penumbral widths are 0.44 cm (bone) and 0.48 cm (water) at a depth of 4 cm.

From figures 10(c)-(d) it is clear that the profile penumbral regions in the lung phantom are larger than those in the water phantom for both the 0.5 × 0.5 cm^2 and 5 × 5 cm^2 field sizes. This is because the increased lateral range of the electrons in the lung material, produces dose reduction and 'rounded' profile shoulders, and increased dose in the profile tail (low dose region) relative to that in water. The 5 ×5 cm^2 penumbral widths for lung and water at the same depth are 1.12 cm and 0.76 cm respectively. Figure 10(d) demonstrates that near the geometric edge, the dose is reduced inside the field and enhanced outside the beam edge. The energetic Compton electrons generated by the megavoltage photon beam inside the beam geometric edge has a longer range and more lateral scattering in lung resulting in a broader penumbral region.

3.6. *Other considerations*

The issue of dose-to-medium, D_m, vs. dose-to-water, $D_{w,}$ is beyond the scope of this work, but a few remarks are in order. The MC method inherently reports D_m. Traditionally, the conversion between D_m and D_w for treatment-planning algorithms that model the patient as water with variable electron density are currently handled using (Bragg-Gray) stopping-power ratios (e.g. Siebers *et al* 2000, Ma and Li 2011). However, Reynaert *et al* (2018) showed that the application of stopping-power ratios for converting from D_m to D_w in, for example, bone media may be invalid; in regions of electronic equilibrium the ratio of mass energy-absorption coefficients should be applied. Further investigation of this topic as well as the clinical implications of conversion between D_m and D_w is warranted.

4. Summary and Conclusions

Computation of absorbed dose, kerma, and photon and electron fluence distributions, using the EGSnrc Monte-Carlo system, have resulted in a more detailed understanding of dose perturbations caused by tissue inhomogeneities (cortical bone and lung-equivalent material) in small and ultra-small fields of 6 and 15 MV photon beams. The main findings are as follows: (a) in bone-equivalent media, dose distributions are primarily impacted by changes in photon beam spectra resulting from beam hardening; (b) in lung-equivalent media dose distributions are primarily impacted by the increased range and lateral scattering of electrons in the lung; (c) from the computation of the absorbed-dose to collision-kerma ratio, D/K_{col}, it has been shown that quasi-CPE is achieved in the water/bone/water phantom at field sizes > 1 × 1 cm^2 and ≥ 5 × 5 cm^2 for 6 MV and 15 MV photons, respectively. In the water/lung/water phantom, field sizes > 5 × 5 cm^2 (6 MV) and ≥ 16 × 16 cm^2 (15 MV) are required to establish quasi-CPE; (d) at 'ultra-small' field sizes the impact of source occlusion coupled with that of

loss of CPE results in significant *dose enhancement* in the bone phantom and *dose reduction* in the lung phantom along the central axis of the beam, being greater at 15 MV than at 6 MV; (e) photon and electron mean energies and R_{csda} values increase as the field size is reduced, with appreciable increases at the smallest field sizes (< 0.75 × 0.75 cm^2) where the effects of loss of CPE and source occlusion are greatest.

Understanding the physics of small fields is of paramount importance in the clinical setting where small fields are frequently employed in treatment planning and dosimetry. The key findings of this study will be useful to clinical physicists dealing with small fields.

Acknowledgements

This work is supported in part by a grant from Varian Medical Systems, Palo Alto, CA. The authors are grateful to Professor Benjamin Movsas, Chair, Department of Radiation Oncology, Henry Ford Health System (HFHS) for his support during this work. SK thanks Drs. Hassan Bagher-Ebadian and Zhen Sun, clinical application developers, HFHS, for installing the EGSnrc Monte Carlo system on PCs. SK is also grateful to Dr. Suneetha Devpura for helpful discussions. SK also thanks Dr. George Georgiou, Physics research group, Clatterbridge Cancer Centre, UK for sharing his expert knowledge of the BEAMnrc system. SK is indebted to Drs. Alison Scott and Tracy Underwood for the use of their 15 MV and 6 MV beam models respectively. SK is also grateful to Gurmeet Singh, Computer Division, Bhabha Atomic Research Centre (BARC), Mumbai, India for helping to develop the software in JAVA for extracting data from EGSnrc output files. SK wishes to thank to Dr. Balvinder Sapra, Head, Radiological Physics & Advisory Division, BARC, Mumbai, India for her encouragement and support. Finally SK expresses his gratitude to BARC, Department of Atomic Energy, Government of India for supporting his secondment to the USA.

References

Alfonso R, Andreo P, Capote R, Huq M S, Kilby W, Kjäll P, Mackie T R, Palmans H, Rosser K, Seuntjens J, Ullrich W and Vatnitsky S 2008 A new formalism for reference dosimetry of small and nonstandard fields *Med. Phys.***35** 5179-86

Andreo P and Nahum A E 1985 Stopping-power ratio for a photon spectrum as a weighted sum of the values for monoenergetic photon beams *Phys. Med. Biol.***30**, 1055-65

Andreo P, Burns D T, Nahum A E, Seuntjens J and Attix F H 2017 *Fundamentals of Ionizing Radiation Dosimetry* (Weinheim, Germany: Wiley-VCH)

Attix F H 1979a The partition of kerma to account for bremsstrahlung *Health Phys*. **36** 347-354

Attix F H 1979b Addendum to the partition of kerma to account for bremsstrahlung *Health Phys*. **36** 536

Attix F H 1986 *Introduction to Radiological Physics and Radiation Dosimetry* (New York: Wiley)

Benmakhlouf H and Andreo P 2017 Spectral distribution of particle fluence in small field detectors and its implication on small field dosimetry *Med. Phys*. **44** 713-724

Berger M J, Hubbell J H, Seltzer S M, Chang J, Coursey J S, Sukumar R, Zucker D S and Olsen K 2010 XCOM: photon cross section database (version 1.5) *Technical Report* NIST, Gaithersburg, MD (http://physics.nist.gov/xcom)

Bouchard H, Seuntjens J, Carrier J F and Kawrakow I 2009 Ionization chamber gradient effects in nonstandard beam configurations *Med. Phys*. **36** 4654-63

Bouchard H, Seuntjens J, Duane S, Kamio Y and Palmans H 2015 Detector dose response in megavoltage small photon beams. I. Theoretical concepts *Med. Phys*. **42** 6033-47

Bjärngard B E, Tsai J S and Rice R K 1990 Doses on the central axes of narrow 6 MV x-ray beams *Med. Phys*. **17** 795-799

Carrasco P, Jornet N, Duch M A, Weber L, Ginjaume M, Eudaldo T, Jurado D, Ruiz A and Ribas M 2004 Comparison of dose calculation algorithms in phantoms with lung equivalent heterogeneities under conditions of lateral electronic disequilibrium *Med. Phys*. **31** 2899-2911

Carrasco P, Jornet N, Duch M A, Panettieri V, Weber L, Eudaldo T, Ginjaume M and Ribas M 2007 Comparison of dose calculation algorithms in slab phantoms with cortical bone equivalent heterogeneities *Med. Phys*. **34** 3323-33

Chetty I J, Charland P M, Tyagi N and McShan D L 2003 Photon beam relative dose validation of the DPM Monte Carlo code in lung-equivalent media *Med. Phys*. **30** 563-573

Chetty I J, Curran B, Cygler J E, DeMarco J J, Ezzell G, Faddegon B A, Kawrakow I, Keall P J, Liu H, Ma C M, Rogers D W O, Seuntjens J, Sheikh-Bagheri D and Siebers J V 2007 Report of the AAPM Task Group No. 105: issues associated with clinical implementation of Monte Carlo-based photon and electron external beam treatment planning *Med. Phys*. **34** 4818-53

Dose, kerma and fluence distributions in heterogeneous slab geometries under non-equilibrium conditions

Das I J and Khan F M 1989 Backscattering dose perturbation at high atomic interface in megavoltage photon beams *Med. Phys.* **16** 367-375

Das I J, Ding G X and Ahnesjö A 2008 Small fields: nonequilibrium radiation dosimetry *Med. Phys.* **35** 206-12

Disher B, Hajdok G, Gaede S and Battista J J 2012 An in-depth Monte Carlo study of lateral electron disequilibrium for small fields in ultra-low density lung: implication for modern radiation therapy *Phys. Med. Biol.***57** 1543-59

Fano U 1954 Note on the Bragg-Gray cavity principle for measuring energy dissipation *Radiat. Res.* **1** 237-40

Fenwick J D, Kumar S, Scott A J D and Nahum A E 2013 Using cavity theory to describe the dependence on detector density of dosimeter response in non-equilibrium small fields *Phys. Med. Biol.***58** 2901-23

Fragoso M, Wen N, Kumar S, Liu D, Ryu S, Movsas B, Munther A and Chetty I J 2010 Dosimetric verification and clinical evaluation of a new commercially available Monte Carlo-based dose algorithm for application in stereotactic body radiation therapy (SBRT) treatment planning *Phys. Med. Biol.* **55** 4445-64

Francescon P, Cora S and Satariano N 2011 Calculation of $k_{Q(clin),Q(msr)}^{f(clin),f(msr)}$ for several small detectors and for two linear accelerators using Monte Carlo simulations. *Med. Phys.* **38** 6513-26

Harder D 1974 Fano's Theorem and the Multiple Scattering Correction. In *Proc. 4th Symp. Microdosimetry* (1973), J. Booz, H. G. Ebert, R. Eickel, and A. Walker (eds.). Verbania Pallanza, Italy, pp. 677–693

Hubbell J H and Seltzer S M 2004 Tables of x-ray mass attenuation coefficients and mass energy-absorption coefficients (version 1.4) http://physics.nist.gov/xaamdi (Gaithersburg, MD: National Institute of Standards and Technology)

IAEA 2008 Measurement uncertainty: a practical guide for secondary standards dosimetry laboratory, *TECDOC-1585* (Vienna: International Atomic Energy Agency)

IAEA 2017 Dosimetry of Small Static Fields Used in Radiotherapy: An International Code of Practice for Reference and Relative Dose Determination *Technical Reports Series 483* (Vienna: International Atomic Energy Agency)

ICRP-23 1975 Reference Man: anatomical, physiological and metabolic characteristic International Commission of Radiation Protection Report 23 (New York: ICRP)

ICRU 1989 Tissue substitute in radiation dosimetry and measurement *Report 44* ((Bethesda, MD: International Commission on Radiation Units and Measurements)

ICRU 1998 Fundamental Quantities and Units for Ionizing Radiation *ICRU Report 60* (Bethesda, MD: International Commission on Radiation Units and Measurements)

ICRU 2016 Key Data for Ionizing-Radiation Dosimetry: Measurement Standards and Applications (Journal of the ICRU vol 14) *ICRU Report 90* (Bethesda, MD: International Commission on Radiation Units and Measurements)

ICRU 2017 Prescribing, Recording, and Reporting of Stereotactic Treatment with Small Photon Beams (Journal of the ICRU vol 14 (2)) *ICRU Report 91* (Oxford University Press, Oxford: International Commission onRadiation Units and Measurements)

IPEM 2010 Small field MV photon dosimetry *IPEM Report 103* (York, UK: Institute of Physics and Engineering in Medicine)

Jones A O, Das I J and Jones F L 2003 A Monte Carlo study of IMRT beamlets in inhomogeneous media *Med. Phys.* **30** 296-300

Kawrakow I, Mainegra-Hing E, Rogers D W O, Tessier F and Walters B R B 2019 The EGSnrc code system: Monte Carlo simulation of electron and photon transport *NRCC Report* PIRS-*701* (Ottawa: National Research Council of Canada): **https://nrc-cnrc.github.io/EGSnrc/doc/pirs701-egsnrc.pdf**

Kumar S, Deshpande D D and Nahum A E 2015a Monte-Carlo-derived insights into dose-kerma-collision kerma inter-relationships for 50 keV to 25 MeV photon beams in water, aluminium and copper *Phys. Med. Biol.* **60** 501-519

Kumar S, Fenwick J D, Underwood T S A, Deshpande D D, Scott A J D and Nahum A E 2015 Breakdown of Bragg-Gray behaviour for low-density detectors under electronic disequilibrium conditions in small megavoltage photon fields *Phys. Med. Biol.* **60** 8187-8212

Latifi K *et al* 2014 Study of 201 non-small cell lung cancer patients given stereotactic ablative radiation therapy shows local control dependence on dose calculation algorithm *Int. J. Radiat. Oncol. Biol. Phys.***88** 1108-13

Li A X, Yu C and Holmes T 2000 A systematic evaluation of air cavity dose perturbation in megavoltage x-ray beams *Med. Phys.* **27** 1011–17

Mackie T R, El-khatib E, Battista J and Scrimger J 1985 Lung dose corrections for 6 MV and 15 MV x-rays *Med. Phys.***12** 327-332

Ma C M and Li J 2011 Dose specification for radiation therapy: dose to water or dose to medium? *Phys. Med. Biol.* **56** 3073-89

Mohan R, Chui C and Lidofsky L 1985 Energy and angular distribution of photons from medical linear accelerators *Med. Phys.***12** 592-597

Nahum A E 1978 Water/air mass stopping power ratios for megavoltage photon and electron beams *Phys. Med. Biol.***23** 24-38

Nahum A E 2007 Principles and Basic Concepts in Radiation Dosimetry, in *Handbook of Radiotherapy Physics: Theory and Practice* ed P Mayles, A E Nahum and J C Rosenwald (London: Taylor & Francis), pp 89-115

Ohri N, Tomé W A, Romero A M, Miften M, Haken R K T, Dawson L A, Grimm J, Yorke E and Jackson A 2018 Local control after stereotactic body radiation therapy for liver tumors *Int. J. Radiat. Oncol. Biol. Phys.* (https://doi.org/10.1016/j.ijrobp.2017.12.288)

Pan H, Simpson D R, Mell L K, Mundt A J and Lawson J D 2011 A survey of stereotactic body radiotherapy use in the United States *Cancer* **117** 4566-72

Reynaert N, van der Marck S C, Schaart D R, Van der Zee W, Van Vliet-Vroegindeweij C, Tomsej M, Jansen J, Heijmen B, Coghe M and De Wagter C 2007 Monte Carlo treatment planning for photon and electron beams *Radiat. Phys. Chem.* **76** 643-86

Reynaert N, Corp F, Sterpin E, Kawrakow I and Palmans H 2018 On the conversion of dose to bone to dose to water in radiotherapy treatment planning systems *Phys. Imaging Radiat. Oncol.* **5** 26-30

Rice R K, Mijnheer B J and Chin L M 1988 Benchmark measurements for lung dose corrections for x-ray beams *Int. J. Radiat. Oncol. Biol. Phys.***15** 399-409

Rogers D W O, Kawrakow I, Seuntjens J P, Walters B R B and Mainegra-Hing E 2019 *NRCC Report No.* PIRS-*702 (rev C): NRC user codes for EGSnrc* (Ottawa: National Research Council of Canada): **https://nrc-cnrc.github.io/EGSnrc/doc/pirs702-egsnrc-codes.pdf**

Rogers D W O and Townson R W 2019 On calculating kerma, collision kerma and radiative yields *Med. Phys.* **46** 5173-84

Rustgi A K, Samuels M A and Rustgi S N 1997 Influences of air inhomogeneities in radiosurgical beams *Med. Dosim.***22** 95-100

Rustgi S N, Rustgi A K, Jiang S B and Ayyangar K M 1998 Dose perturbation caused by high-density inhomogeneities in small beams in stereotactic radiosurgery *Phys. Med. Biol.***43** 3509-18

Sánchez-DobladoF, Hartmann G H, Pena J, Rosello J V, Rusiello G and Gonzalez-Castao D M 2007 A new method for output factor determination in MLC shaped narrow beams *Phys. Medica* **23** 58-66

Scott A J D, Nahum A E and Fenwick J D 2008 Using a Monte Carlo model to predict dosimetric properties of small radiation fields *Med. Phys.* **35** 4671-84

Scott A J D, Nahum A E and Fenwick J D 2009 Monte Carlo modeling of small photon fields: quantifying the impact of focal spot size on source occlusion and output factors, and exploring miniphantom design for small-field measurements *Med. Phys.* **36** 3132-44

Scott A J D, Kumar S, Nahum A E and Fenwick J D 2012 Characterizing the influence of detector density on dosimeter response in non-equilibrium small photon fields *Phys. Med. Biol.***57** 4461-76

Siebers J V, Keall P J, Nahum A E and Mohan R 2000 Converting absorbed dose to medium to absorbed dose to water for Monte Carlo based photon beam dose calculations *Phys. Med. Biol.***45** 983-95

Underwood T S A, Winter H C, Hill M A and Fenwick J D 2013 Detector density and small field dosimetry: Integral versus point dose measurement schemes *Med. Phys.***40** 082102

Dose, kerma and fluence distributions in heterogeneous slab geometries under non-equilibrium conditions

Figure Captions

Figure 1. Schematic diagram illustrating the calculation geometries with bone-equivalent and lung-equivalent material in bone-equivalent and lung-equivalent cylindrical slab phantoms respectively (A – bone; B – lung). The edges of the wide field and small field are indicated with bold and dashed lines respectively.

Figures 2(a)-(d). Absorbed dose versus field size computed in a water-inhomogeneity-water phantom from the surface to the maximum depth (0 - 30 cm) along the central axis of the beam. with square field sizes ranging from 0.25 × 0.25 cm^2 to 7 × 7 cm^2 at 6 MV photon beam (a – bone; c – lung) and 0.25 × 0.25 cm^2 to 16 × 16 cm^2 at 15 MV photon beam (b – bone; d – lung) defined at 100 cm SSD.

Figure 3. Electron fluence, differential in energy (all generations), for 6 MV photon beam computed at 2.95 cm depth in the bone-equivalent slab phantom as well as in the homogeneous (water) phantom : 0.25 × 0.25 cm^2, 100 cm SSD, homogeneous water – – – – –; bone slab from 3 to 5 cm depth ——.

Figure 4(a). Monte-Carlo-derived ratios of absorbed dose to collision kerma (D/K_{col}) at the centre of a bone slab (3 – 5 cm depth) in water and in homogeneous water on the central axis at 3.975 cm depth in a cylindrical phantom for a 6 MV photon beam at square field sizes (defined at 100 cm source-to-phantom surface distance) of side lengths 0.25, 0.5, 0.75, 1, 2, and 3 cm; **(b)** same quantities and media for a 15 MV photon beam; extending to 10 cm side length. The error bars are ± 2 standard deviations and correspond to Type A uncertainties.

Figure 4(c). Monte-Carlo-derived ratios of absorbed dose to collision kerma (D/K_{col}) at the centre of a lung slab (3 – 10 cm depth) in water and in homogeneous water on the central axis at 6.475 cm depth in a cylindrical phantom for a 6 MV photon beam at square field sizes (defined at 100 cm source-to-phantom surface distance) of side lengths 0.25, 0.5, 0.75, 1, 2, 3, 5, 5.5, 6 and 7cm; **(d)** same quantities and media for a 15 MV photon beam; extending to 16 cm side length. The error bars are ± 2 standard deviations and correspond to Type A uncertainties.

Figure 5. Total photon fluence, differential in energy, along the central axis, normalized to the fluence at the incident energy, for a 15 MV photon beams, at depth 3.975 cm in bone medium located in heterogeneous phantom (bone-equivalent slab phantom) versus field size defined at 100 SSD; side lengths of square fields are 0.25 cm, 0.45 cm, 1 cm, 2cm, 3 cm and 5cm.

Figures 6(a)–(d). The MC-derived dose perturbation factors, *DPF's* computed from equation (4) in a water-inhomogeneity-water phantom from the surface to the maximum depth (0 - 30 cm) along the central axis of the beam. with square field sizes ranging from 0.25 × 0.25 cm^2 to 7 × 7cm^2 at 6 MV photon beam (a – bone; c – lung) and 0.25 × 0.25 cm^2 to 16 × 16 cm^2 at 15 MV photon beam (b – bone; d – lung) defined at 100 cm SSD.

Figure 7(a). 6 MV photons**,** 0.25 × 0.25 cm^2 field size defined at 100 cm SSD: primary electron fluence (per MeV per incident particle) as a function of electron kinetic energy (MeV) scored in i) a 'point like' bone voxel (0.5 mm diameter, 0.5 mm thickness), ii) a 'point like' water voxel, and iii) the fluence in ii) $\times\left(p_{\Phi}\right)_{\text{water}}^{\text{bone}}$ (= 1.231); both scoring volumes positioned at 3.975 cm depth along the beam central axis in a heterogeneous phantom (bone-equivalent slab phantom) and homogeneous (water) phantom respectively .

Figure 7(b). 15 MV photons**,** 0.25 × 0.25 cm^2 field size defined at 100 cm SSD: primary electron fluence (per MeV per incident particle) as a function of electron kinetic energy (MeV) scored in i) a 'point like' bone voxel (0.5 mm diameter, 0.5 mm thickness), ii) a 'point like' water voxel, and iii) the fluence in ii) $\times\left(p_{\Phi}^{\text{prim}}\right)_{\text{w}}^{\text{bone}}$ (= 1.403); both scoring volumes positioned at 3.975 cm depth along the beam central axis in a heterogeneous phantom (bone-equivalent slab phantom) and homogeneous (water) phantom respectively.

Figure 7(c). 15 MV photons**,** 2 × 2 cm^2 field size defined at 100 cm SSD: Primary electron fluence (per MeV per incident particle) as a function of electron kinetic energy (MeV) scored in i) a 'point like' bone voxel (0.5 mm diameter, 0.5 mm thickness), ii) a 'point like' water voxel, and iii) the fluence in ii) $\times\left(p_{\Phi}^{\text{prim}}\right)_{\text{w}}^{\text{bone}}$ (= 1.188); both scoring volumes positioned at 3.975 cm depth along the beam central axis in a heterogeneous phantom (bone-equivalent slab phantom) and homogeneous (water) phantom respectively.

Figure 7(d). 15 MV photons**,** 0.25 × 0.25 cm^2 field size defined at 100 cm SSD: primary electron fluence (per MeV per incident particle) as a function of electron kinetic energy (MeV) scored in i) a 'point like' water voxel (0.5 mm diameter, 0.5 mm thickness), ii) a 'point like' lung voxel, and iii) the fluence in ii) $\times\left(p_{\Phi}^{\text{prim}}\right)_{\text{lung}}^{\text{w}}$ (= 3.003); both scoring volumes positioned at 6.475 cm depth along the beam central axis in a homogeneous (water) phantom and heterogeneous phantom (lung-equivalent slab phantom) respectively.

Figure 8(a). Mean (secondary) electron energy at the central axis in the bone-equivalent slab phantom as a function of depth and field size defined at 100 cm SSD for 6 MV photon beams; side length of square fields are 0.25, 0.5, 0.75, 1, 2and 3 cm.

Figure 8(b). Mean (secondary) electron energy at the central axis in the lung-equivalent slab phantom as a function of depth and field size defined at 100 cm SSD for 6 MV photon beams; side length of square fields are 0.25, 0.5, 0.75, 1, 2 and 3 cm.

Figure 9. Total photon fluence, differential in energy, along the central axis, normalized to the fluence at the incident energy, for a 6 MV photon beams, at depths 1.975 cm, 6.975 cm, 9.975 cm and 14.9 cm in water medium in heterogeneous phantom (bone-equivalent slab phantom) for a 0.25 × 0.25 cm^2 field size defined at 100 cm SSD.

Figures 10(a)-(d). 6 MV photon beam: Comparison of transverse (cross-plane) beam profile generated at the depth of 4 cm (3-5 cm depth, bone slab) and 7 cm depth (3-10 cm depth, lung slab) in bone-equivalent and lung-equivalent slab phantoms respectively with the profile at same depths in homogeneous phantom with square field sizes ranging from 0.5 × 0.5 to 5 × 5 cm^2 defined at 100 cm SSD. All profiles were normalized to absorbed dose per incident fluence computed at d_{max} for a 10 × 10 cm^2 field size in a homogeneous (water) phantom.

Dose, kerma and fluence distributions in heterogeneous slab geometries under non-equilibrium conditions

Table Captions

Table 1. Summary of EGSnrc parameters used in the simulations.

Table 2. Material details as modelled in the MC simulations: the percentage atomic composition of the mass density (ρ) and mean excitation energy of the materials involved in the present work.

Table 3. 6 MV and 15 MV photon beams: $\overline{g} = \left(1 - \left(K_{\text{col}}/K\right)\right)$ determined at depths of 3.975 cm (cortical bone) and 6.475 cm (lung and water), versus field size defined at 100 SSD; lengths of square fields were 0.25 cm, 0.5 cm, 0.75 cm, 1 cm, 2 cm, 3 cm, 5cm, 10 cm and 16 cm; the Type A uncertainties are ± 1 standard deviation.

Table 4. 6 MV and 15 MV photon beams: MC-derived primary electron fluence perturbation correction factors, bone-to-water, $\left(p_{\Phi}\right)_{\text{w}}^{\text{bone}}$ and lung-to-water, $\left(p_{\Phi}\right)_{\text{w}}^{\text{lung}}$, versus field size defined at 100 cm SSD; side lengths of square fields were 0.25 cm, 0.5 cm, 0.75 cm, 1 cm, 2 cm, 3 cm, 5cm, 10 cm and 16 cm; the Type A uncertainties are ± 2 standard deviations.

Table 5. 6 MV and 15 MV photon beams: comparison of MC-derived dose perturbation factors med-to-water to primary electron fluence perturbation correction factors med-to-water, $\left[DPF(z)\right]_{\text{w}}^{\text{med}} / \left(p_{\Phi}^{\text{prim}}\right)_{\text{w}}^{\text{med}} \simeq s_{\text{med,w}}^{\text{BG}}$ i.e. equations (9) and (10) at depth 3.975 (med = bone) and 6.475 cm depth (med= lung) with $\left(s_{\text{med,w}}^{\text{BG}}\right)_{\text{cav th}} = \left[S_{\text{el}}(\overline{E})/\rho\right]_{\text{med}} / \left[S_{\text{el}}(\overline{E})/\rho\right]_{\text{w}}$ determined from the ESTAR code/program. $\overline{E}$ is the fluence-weighted mean energy determined from the 'primary' electron (+ positron) fluence spectra generated by FLURZnrc at 3.975 cm depth and 6.475 cm depth in bone-equivalent and lung-equivalent slab phantoms respectively for the beam qualities of 6 MV and 15 MV. The Type A uncertainties are ± 2 standard deviations.

Table 6. Comparison of $\left(s_{\text{bone,w}}^{\text{BG}}\right)_{\text{Eq.(9)}}$ and $\left(s_{\text{lung,w}}^{\text{BG}}\right)_{\text{Eq.(10)}}$ determined at 3.975 cm depth and 6.475 cm depth in bone-equivalent and lung-equivalent slab phantoms respectively using equations (9) and (10) respectively with the $s_{\text{bone,w}}^{\text{BG}}$ and $s_{\text{lung,w}}^{\text{BG}}$ derived by Siebers *et al* (2000), for 10 × 10 cm^2 field defined at 100 cm SSD for 6 MV and 15 MV. The uncertainties in the present work are ± 2 standard deviations.

Table 7. Mean photon energy, $\overline{E}_k$ (evaluated from equation (11) by replacing $\Phi_E^{tot}(z)$ by 'total' photon fluence, $\Phi_k^{phot}(z)$ in the numerator as well as in the denominator). and (total) electron (+positron) energy, $\overline{E}$ (evaluated from equation (11) using 'total' electron (+ positron) fluence spectra (i.e. including all generations of delta-rays)), at 3.975 cm in bone on central axis of bone-equivalent slab phantom versus field size defined at 100 SSD for 6 MV and 15 MV photon beams; side lengths of square fields were 0.25 cm, 0.5 cm, 0.75 cm, 1 cm, 2 cm, and 3 cm for 6 MV and 0.25 cm, 0.5 cm, 0.75 cm, 1 cm, 2 cm, and 3 cm, 5cm and 10 cm for 15 MV; the Type A uncertainties are ± 1 standard deviation. R_{csda} is quoted for bone medium corresponding to (total) electron (+positron) mean energies.

Table 8. Mean photon energy, $\overline{E}_k$ (evaluated from equation (11) by replacing $\Phi_E^{tot}(z)$ by 'total' photon fluence, $\Phi_k^{phot}(z)$ in the numerator as well as in the denominator). and (total) electron (+positron) energy, $\overline{E}$ (evaluated from equation (11) using 'total' electron (+ positron) fluence spectra (i.e. including all generations of delta-rays)), at 6.475 cm in lung on central axis of lung-equivalent slab phantom versus field size defined at 100 SSD for 6 MV and 15 MV photon beams; side lengths of square fields were 0.25 cm, 0.5 cm, 0.75 cm, 1 cm, 2 cm, 3 cm and 5 cm for 6 MV and 0.25 cm, 0.5 cm, 0.75 cm, 1 cm, 2 cm, and 3 cm, 10 cm and 16 cm for 15 MV; the Type A uncertainties are ± 1 standard deviation. R_{csda} is quoted for lung medium corresponding to (total) electron (+positron) mean energies.

Dose, kerma and fluence distributions in heterogeneous slab geometries under non-equilibrium conditions

Figure 1.

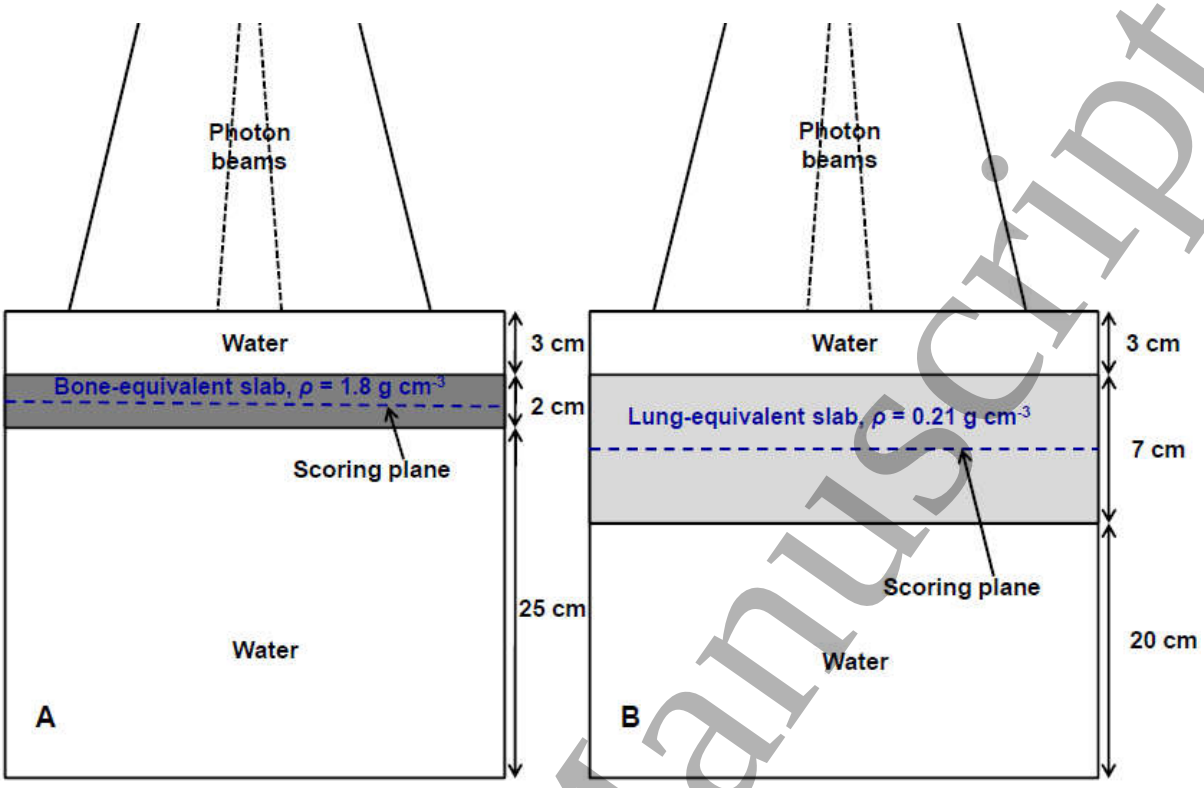

Dose, kerma and fluence distributions in heterogeneous slab geometries under non-equilibrium conditions

Figure 2(a).

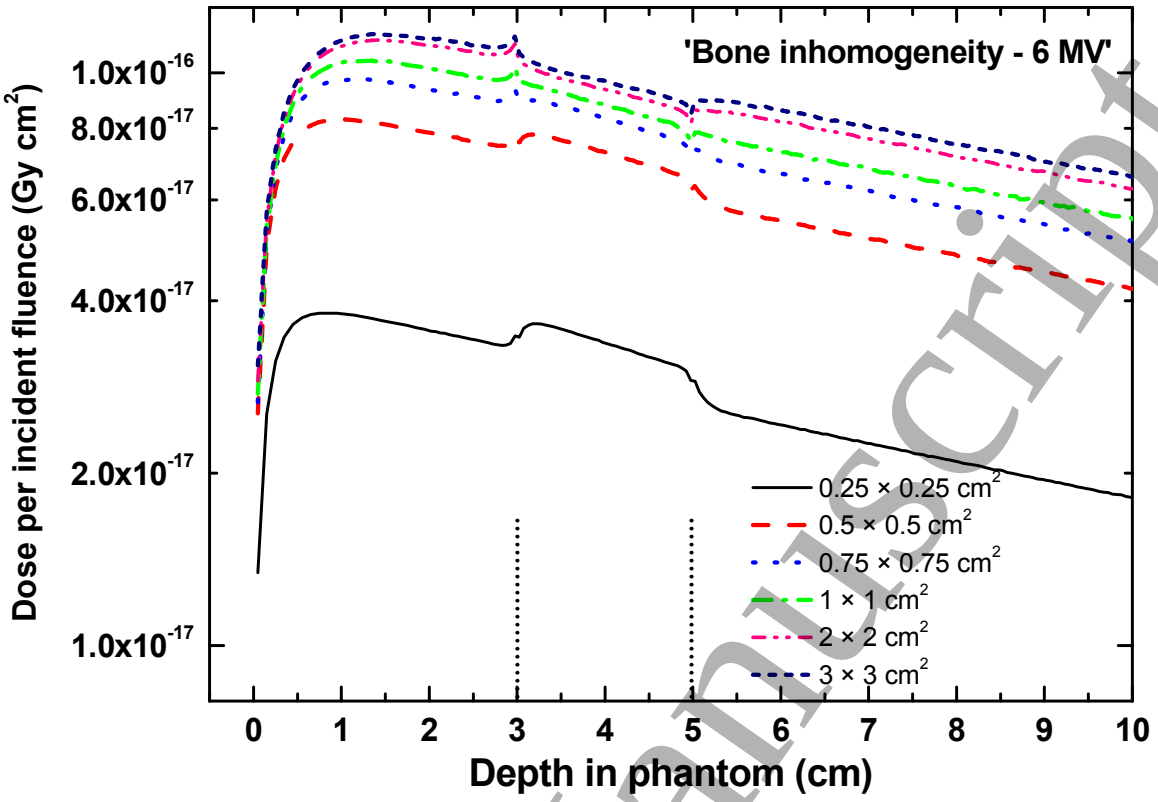

Figure 2(b).

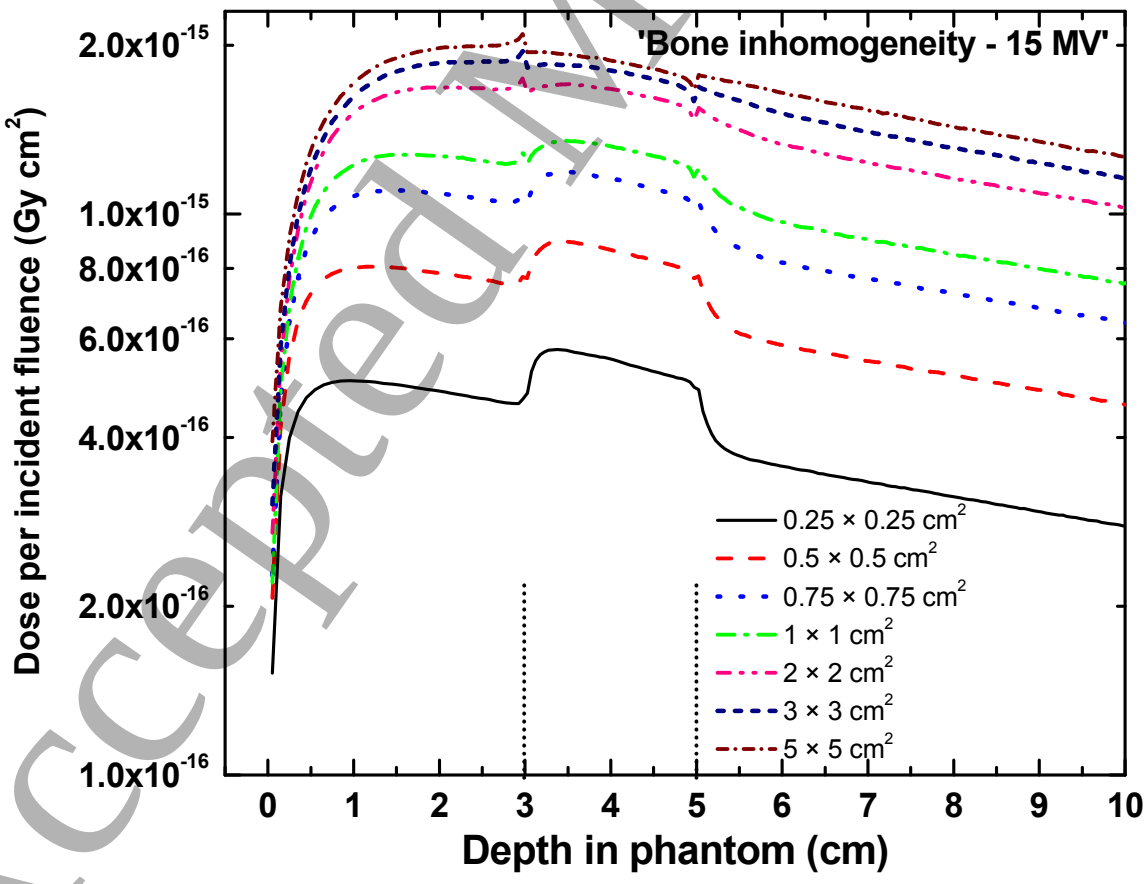

Figure 2(c).

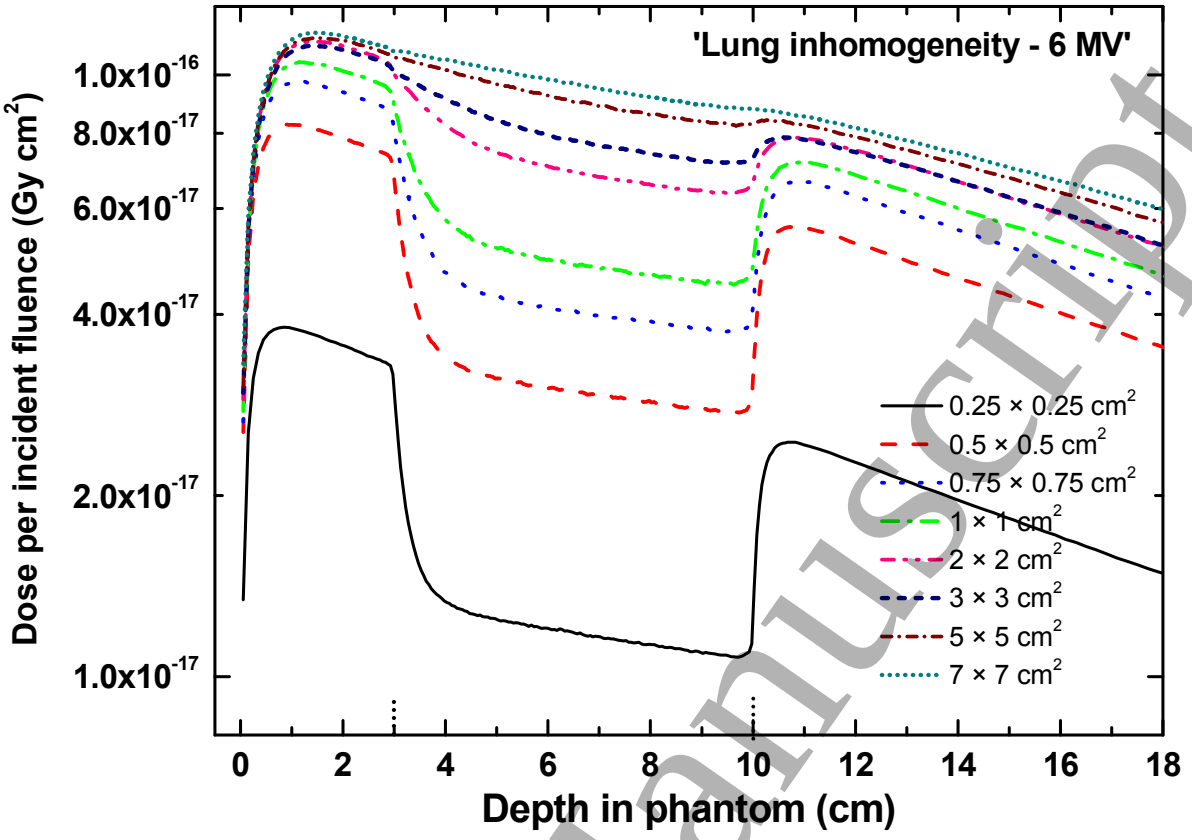

Figure 2(d).

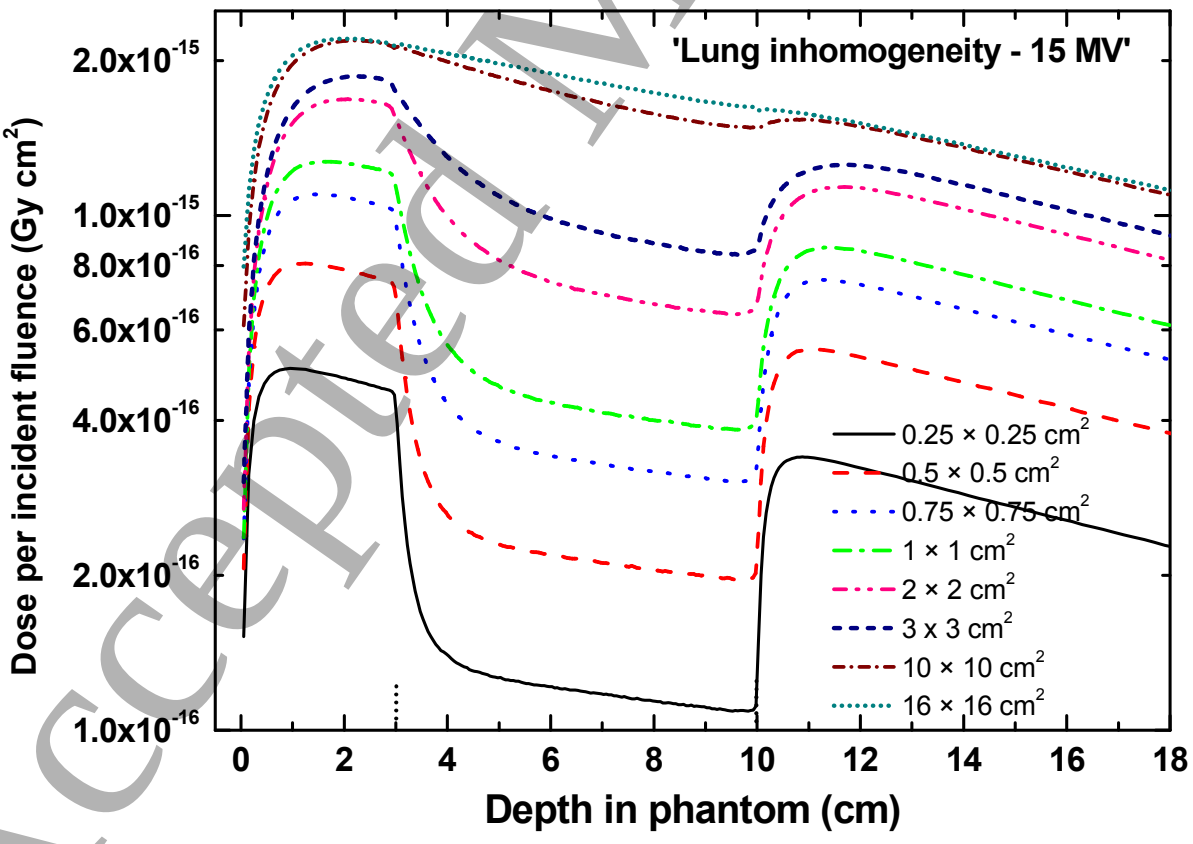

Dose, kerma and fluence distributions in heterogeneous slab geometries under non-equilibrium conditions

Figure 3.

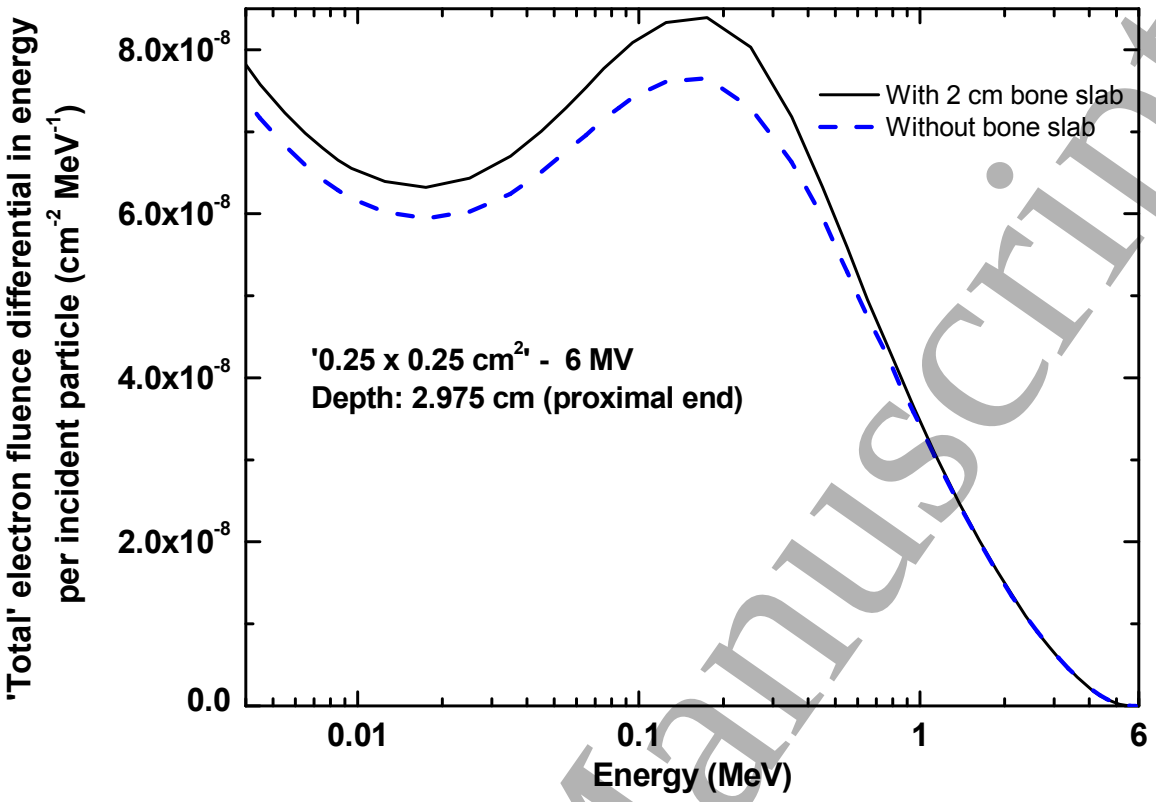

Figure 4(a).

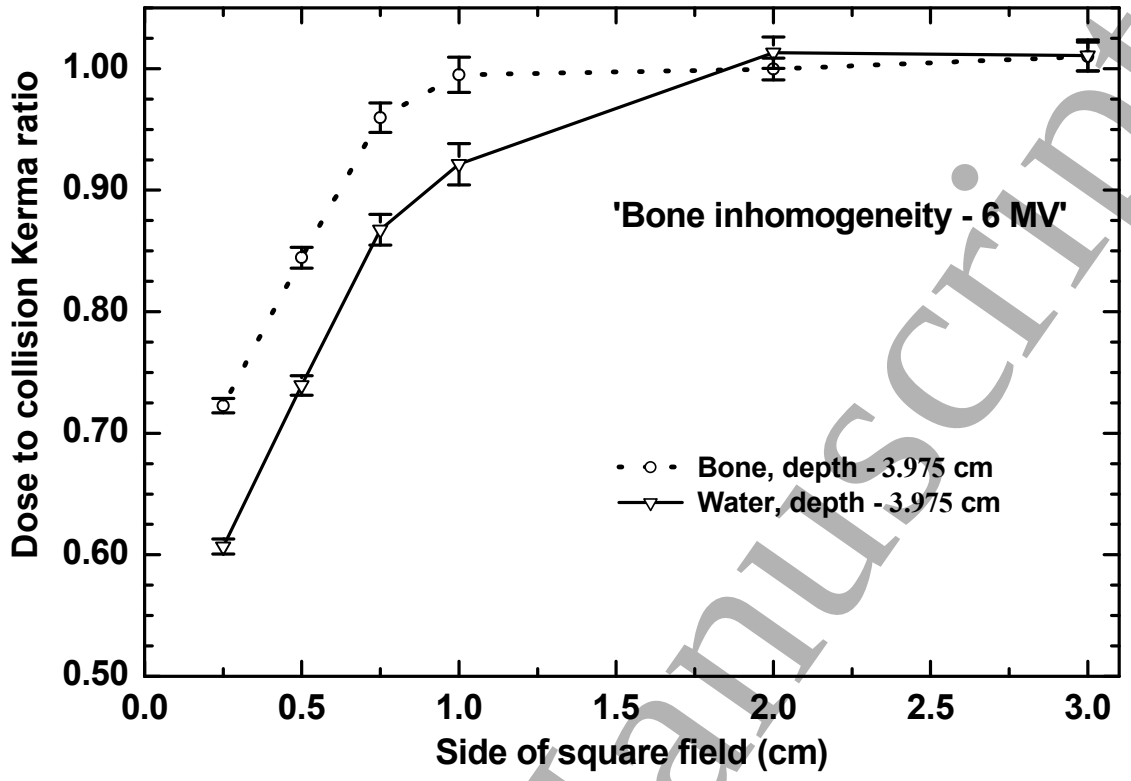

Figure 4(b).

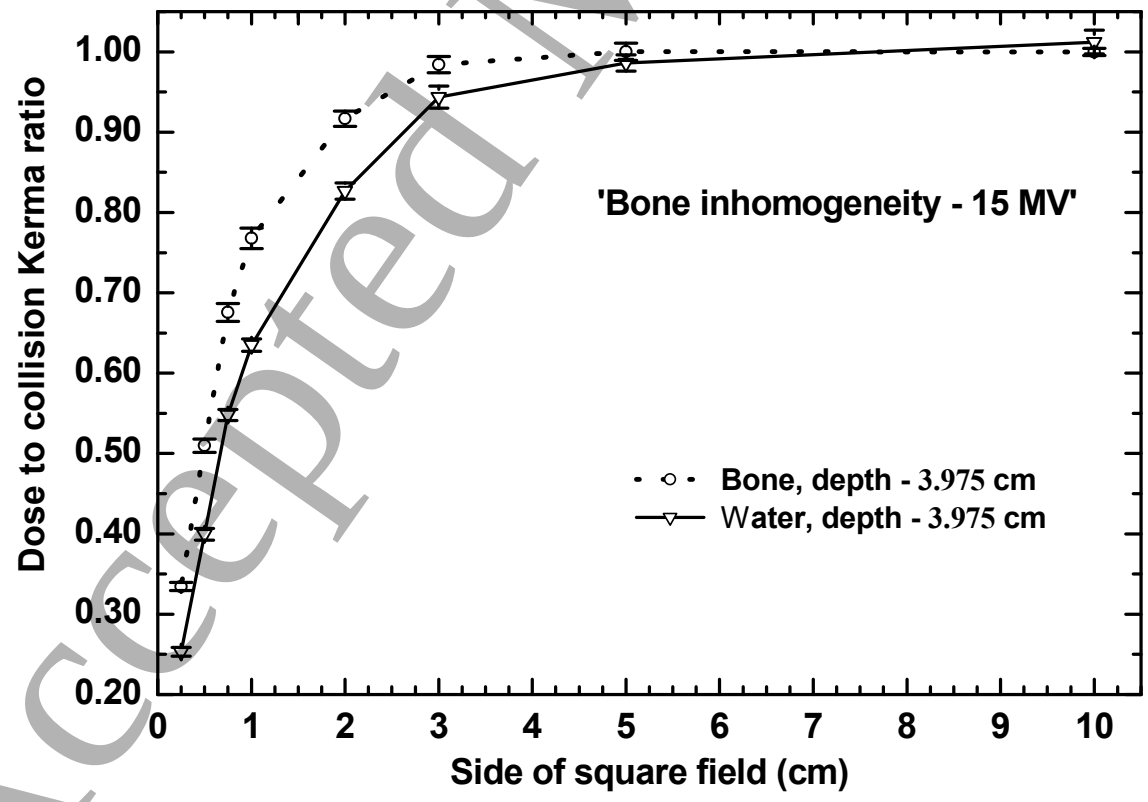

Dose, kerma and fluence distributions in heterogeneous slab geometries under non-equilibrium conditions

Figure 4(c).

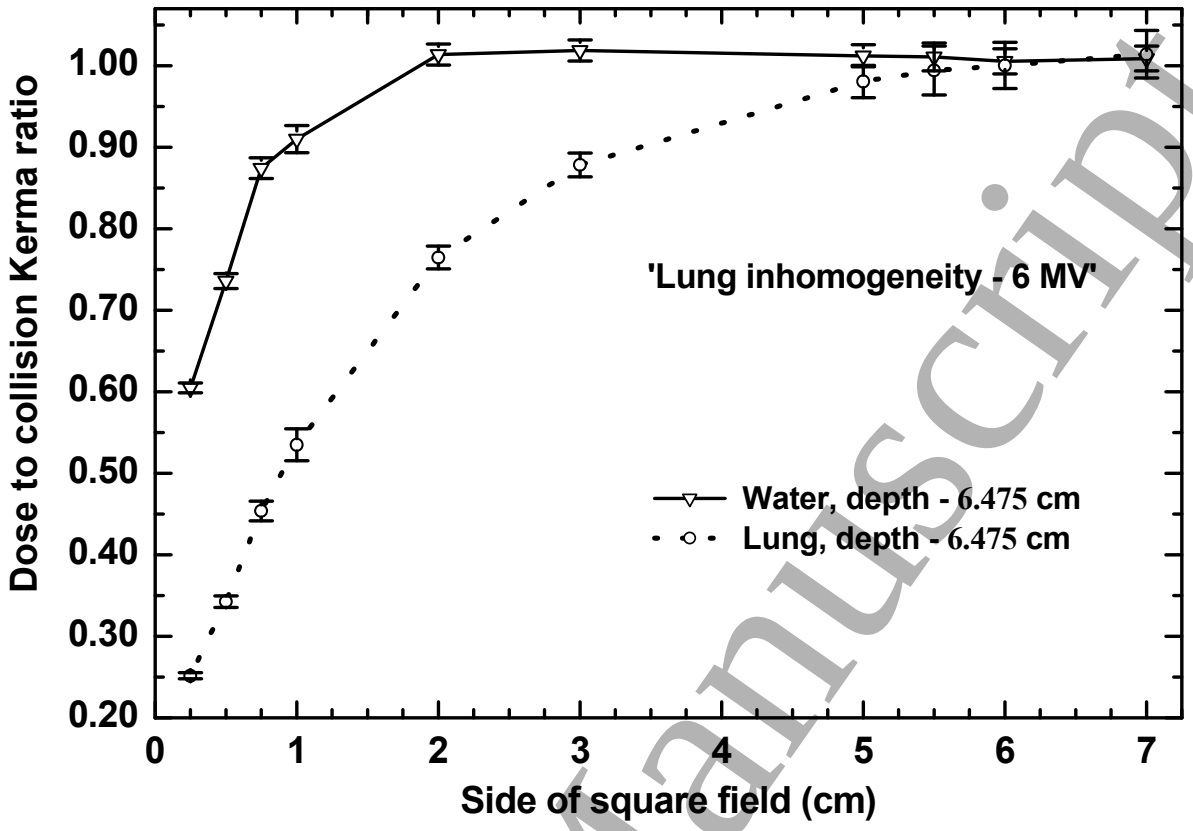

Figure 4(d).

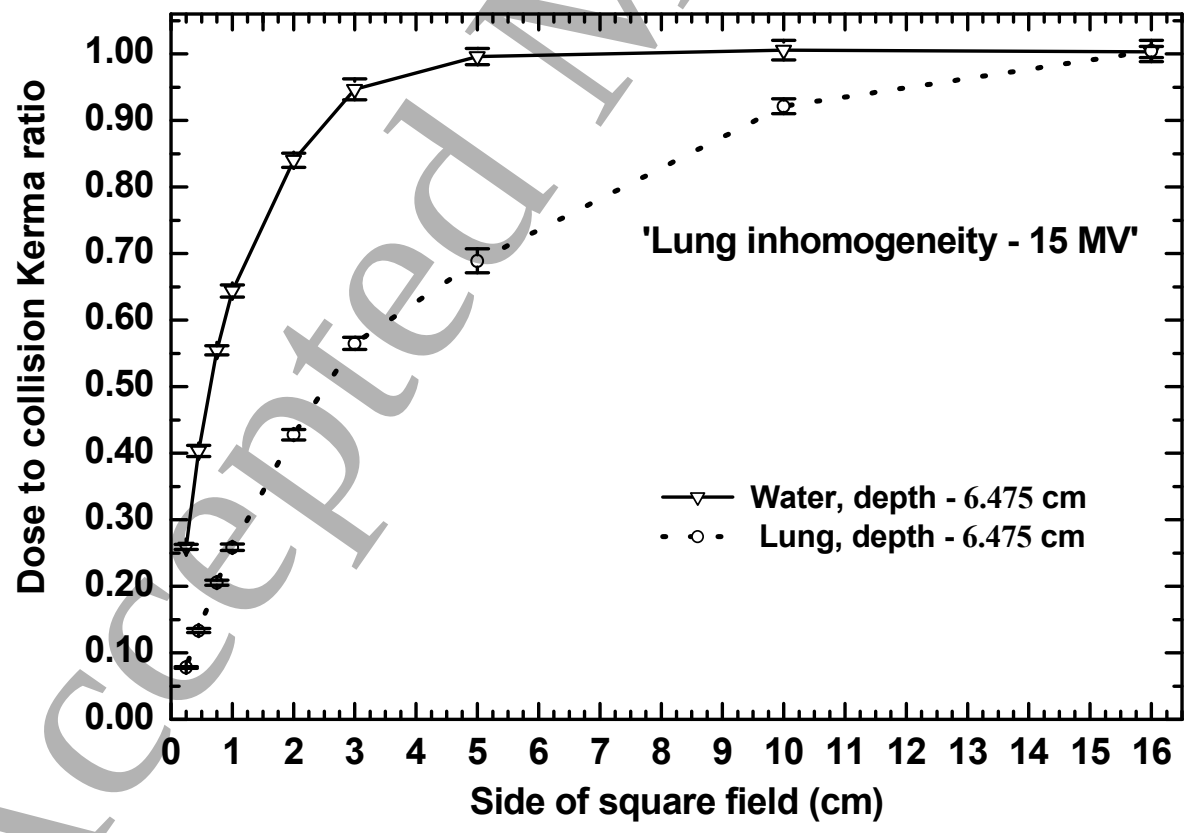

Dose, kerma and fluence distributions in heterogeneous slab geometries under non-equilibrium conditions

Figure 5.

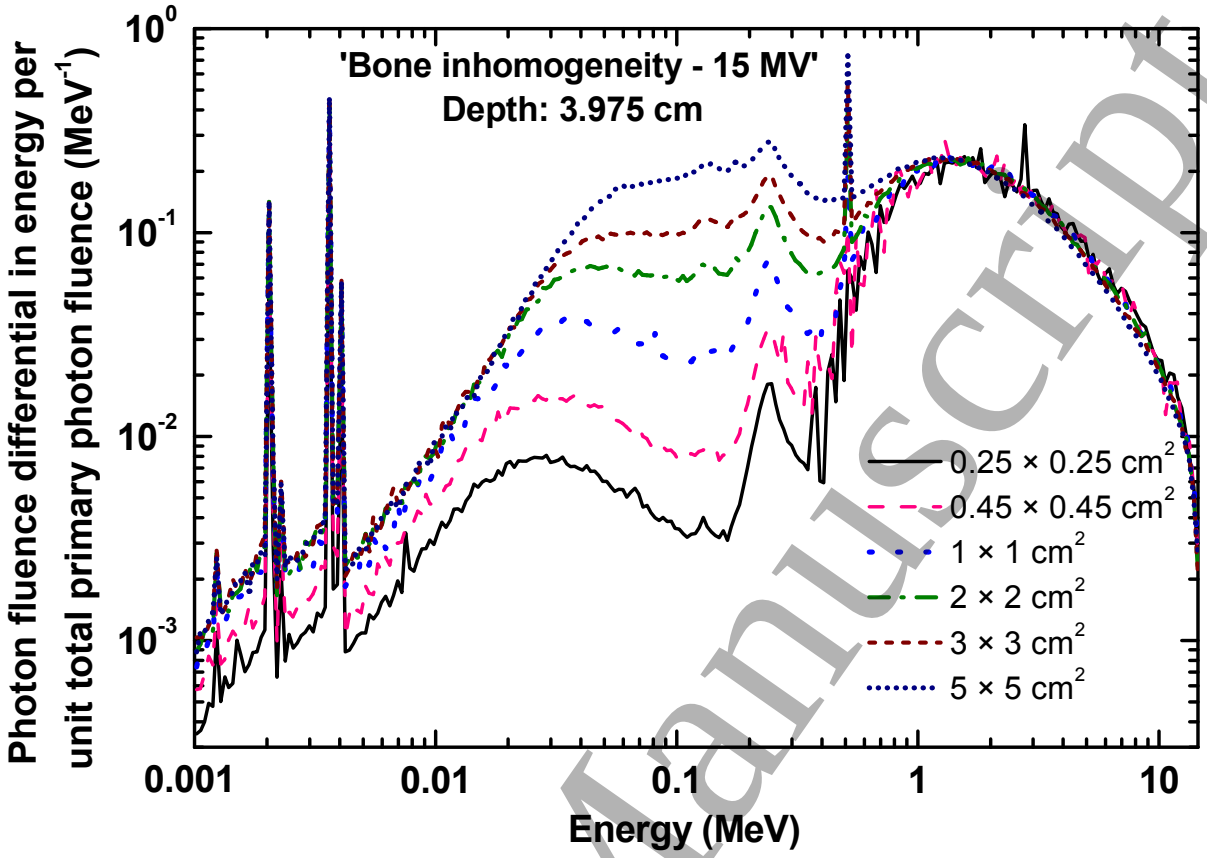

Dose, kerma and fluence distributions in heterogeneous slab geometries under non-equilibrium conditions

Figure 6(a).

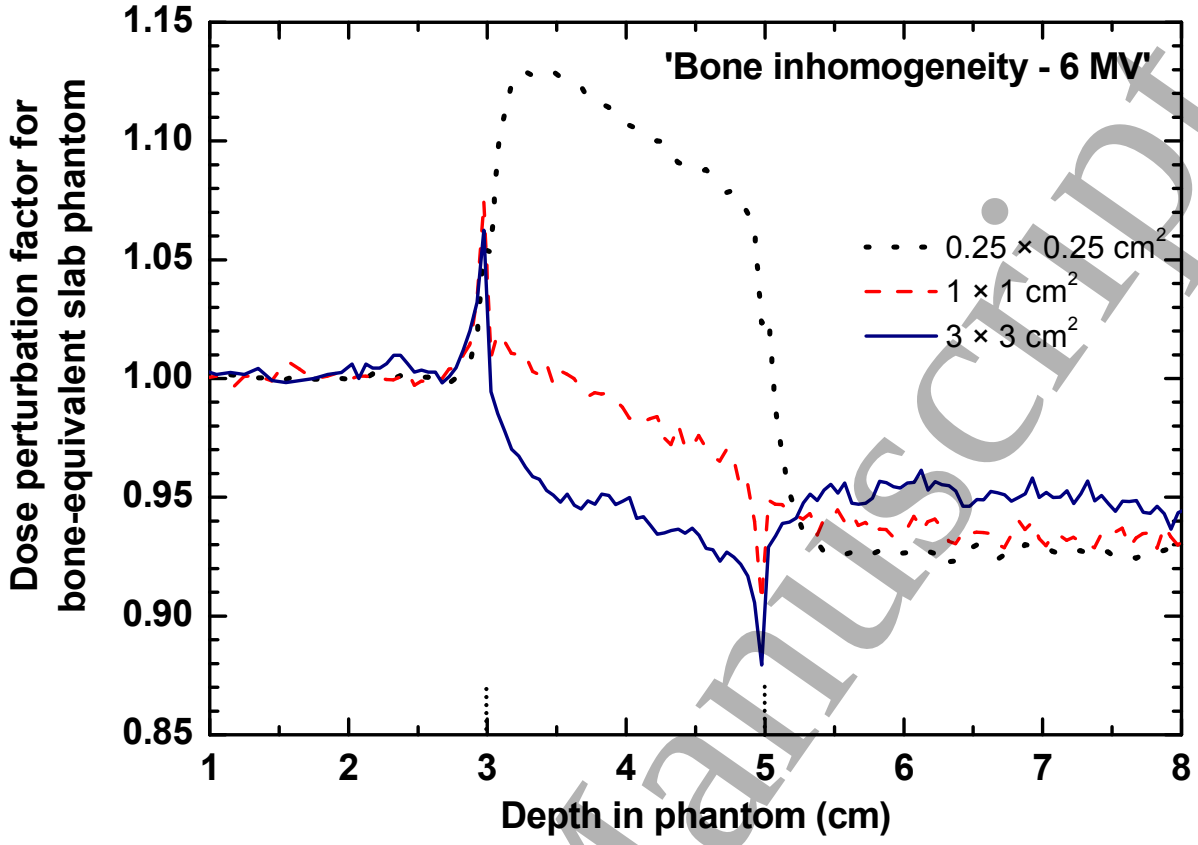

Figure 6(b).

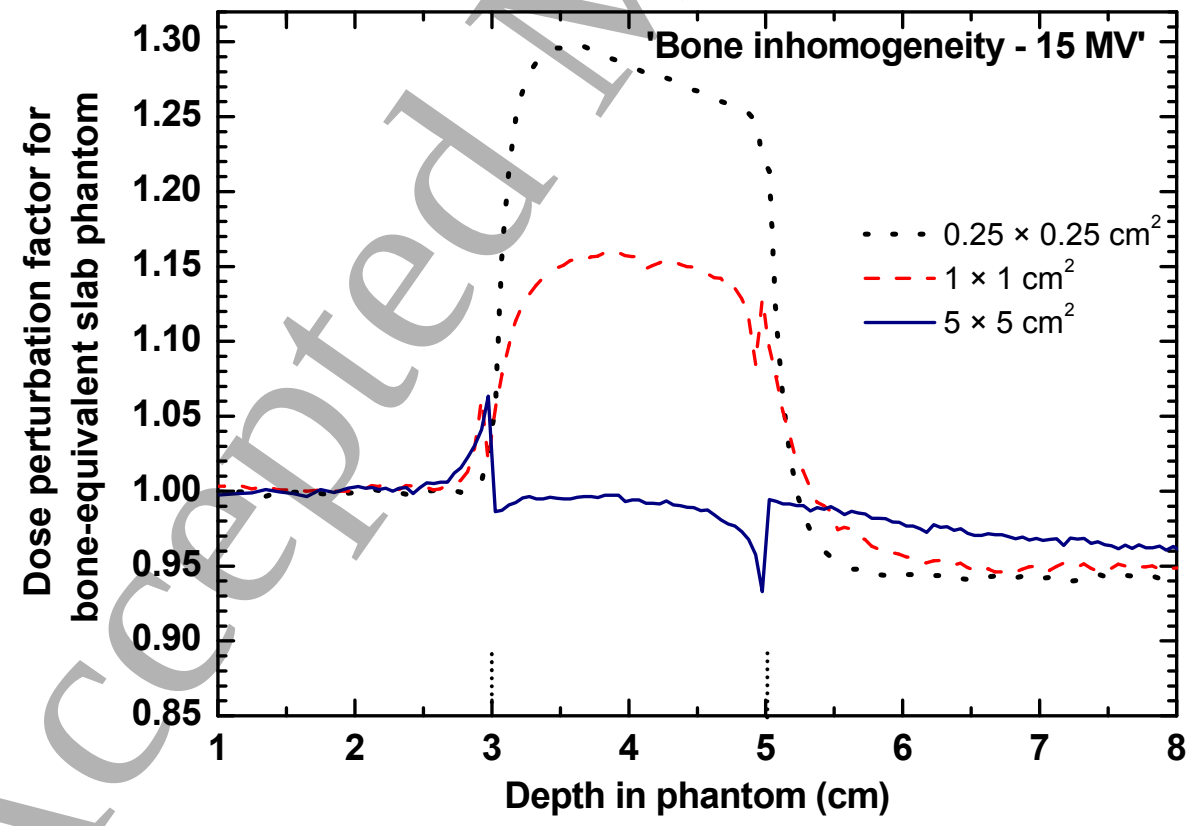

Figure 6(c).

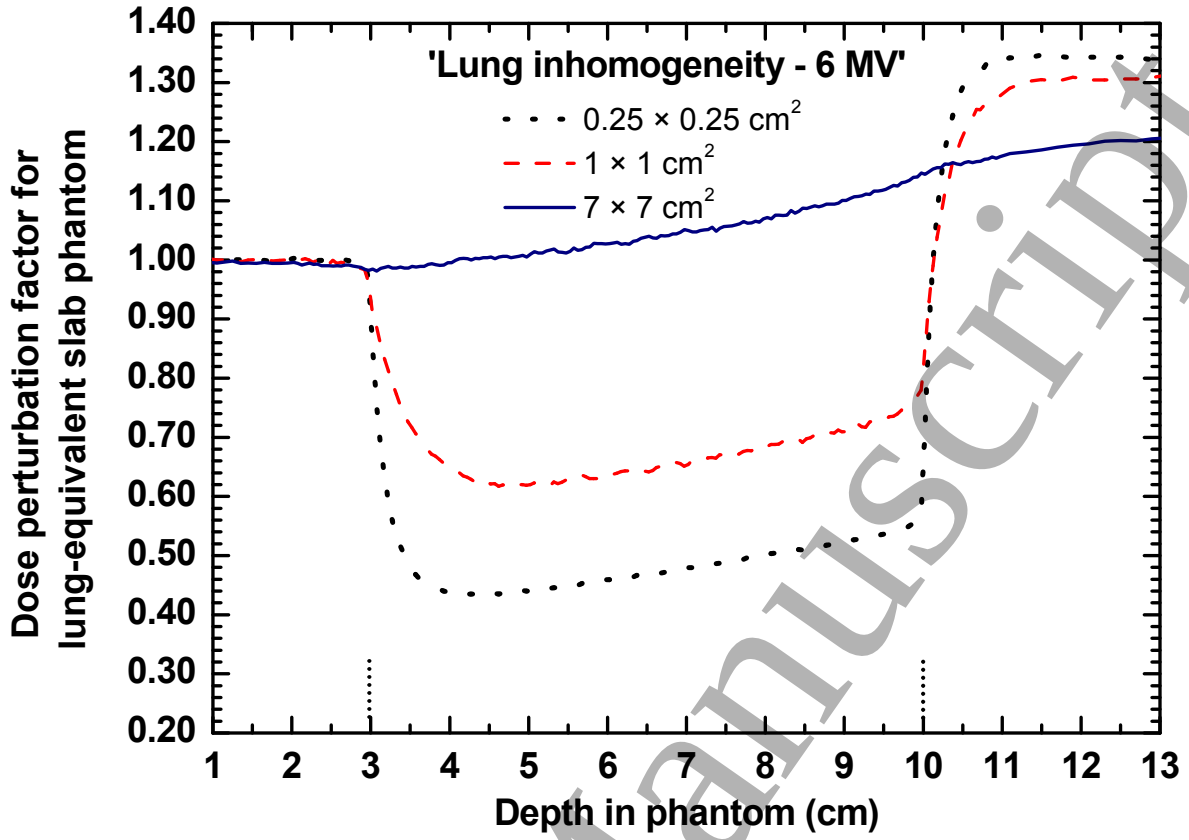

Figure 6(d).

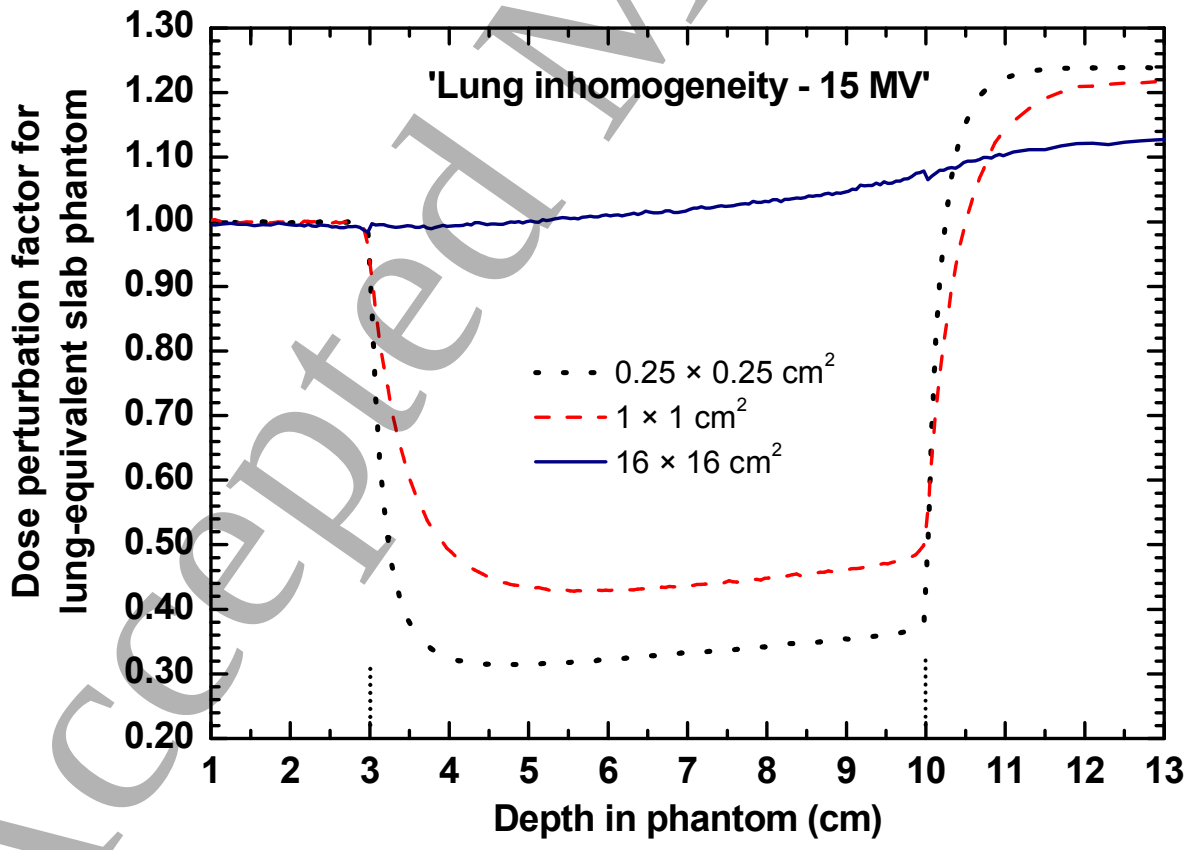

Dose, kerma and fluence distributions in heterogeneous slab geometries under non-equilibrium conditions

Figure 7(a).

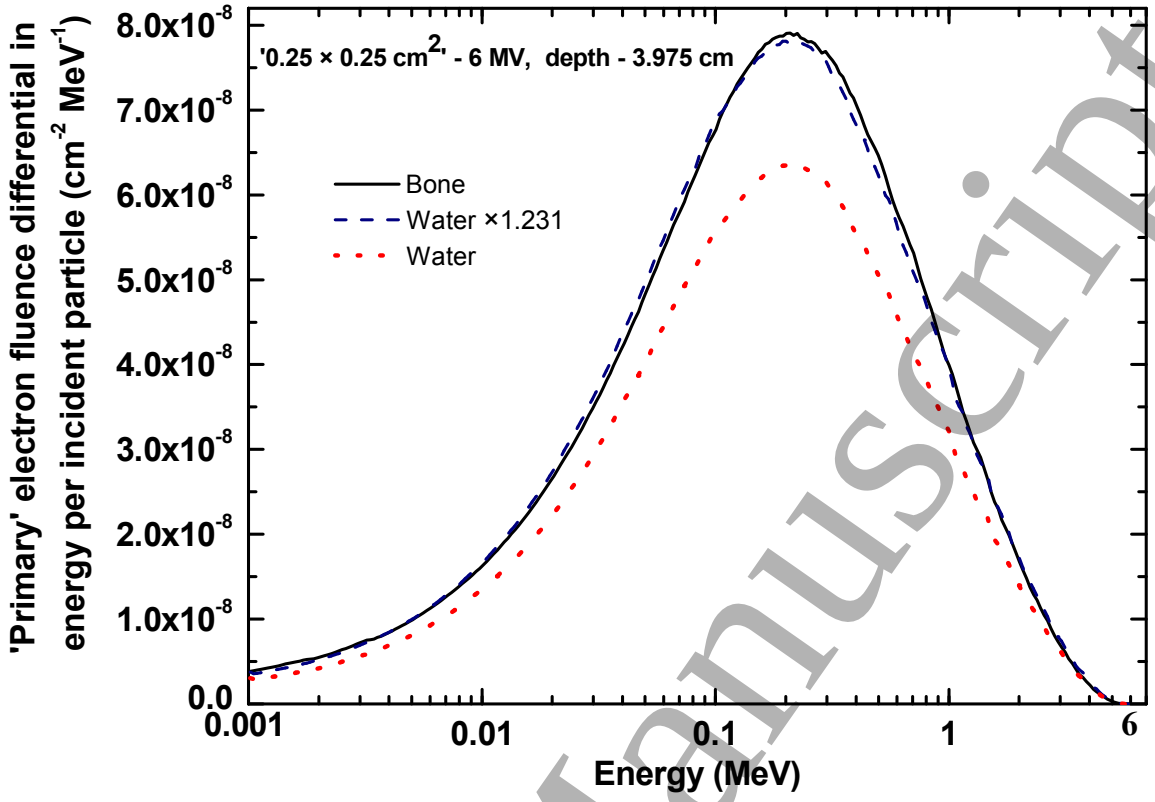

Figure 7(b).

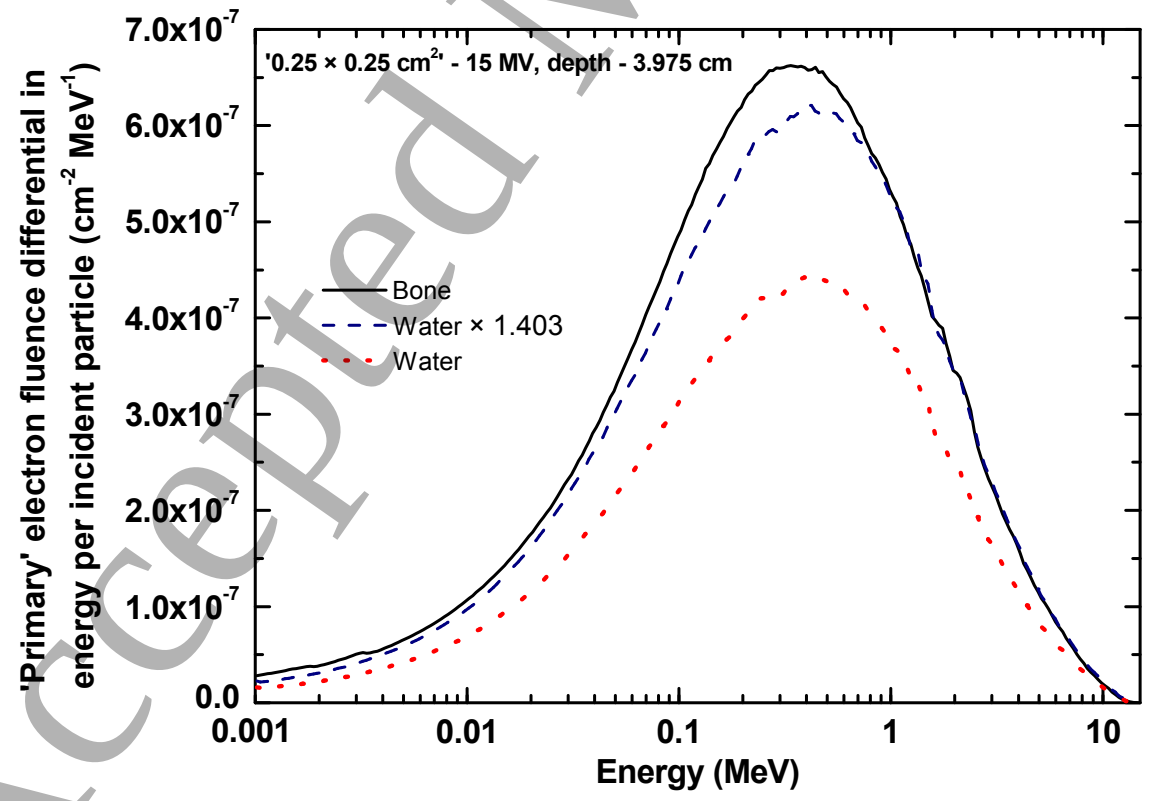

Figure 7(c).

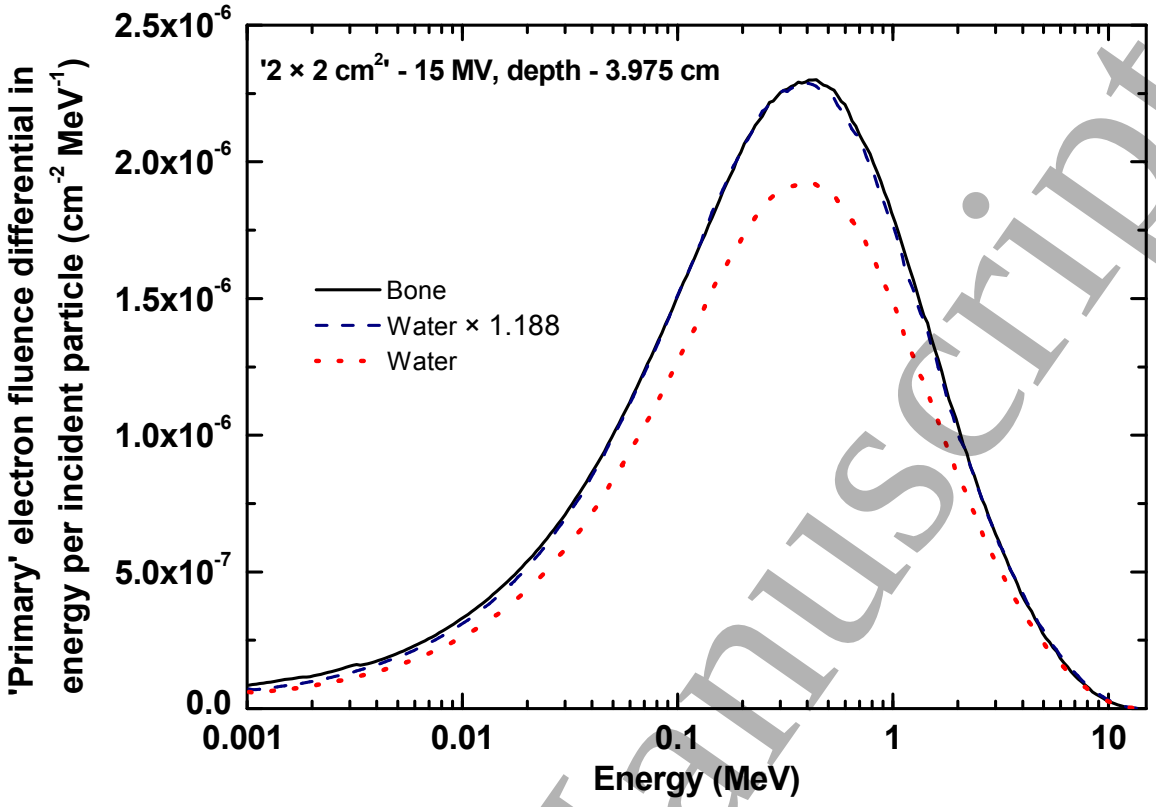

Figure 7(d).

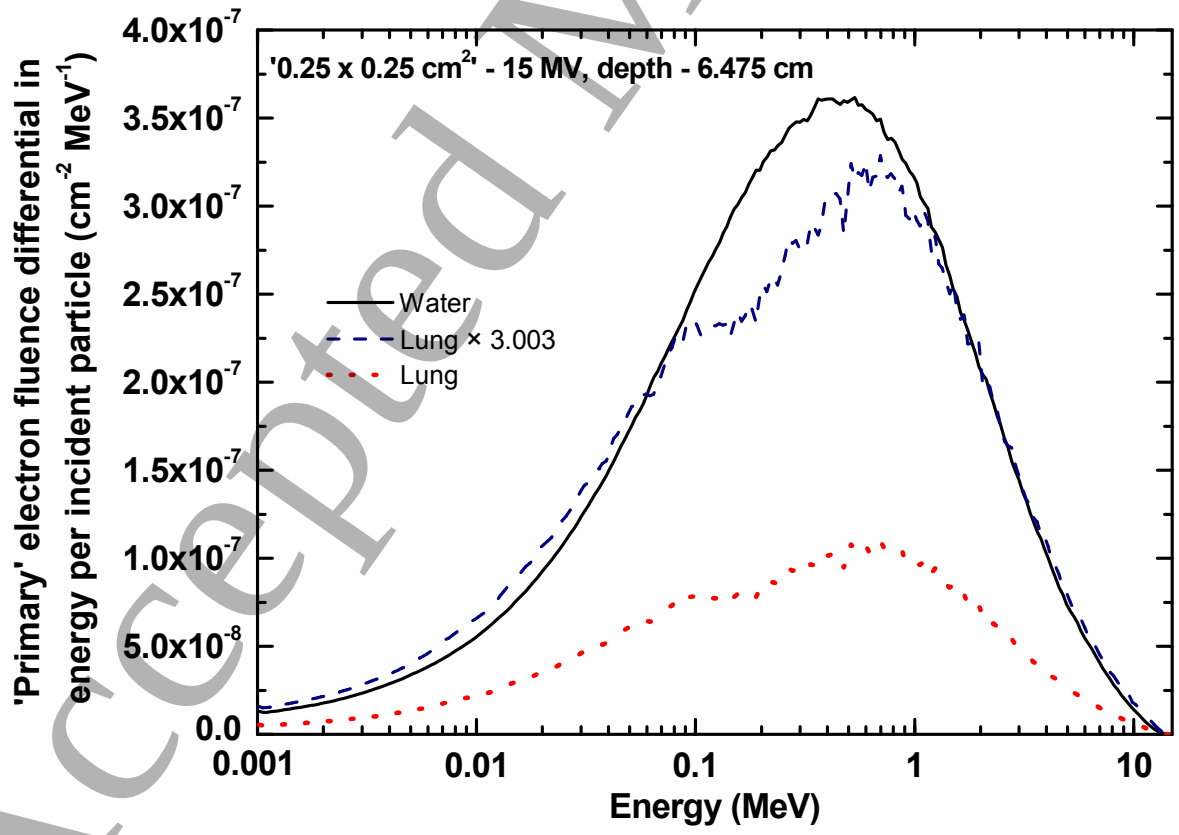

Figure 8(a).

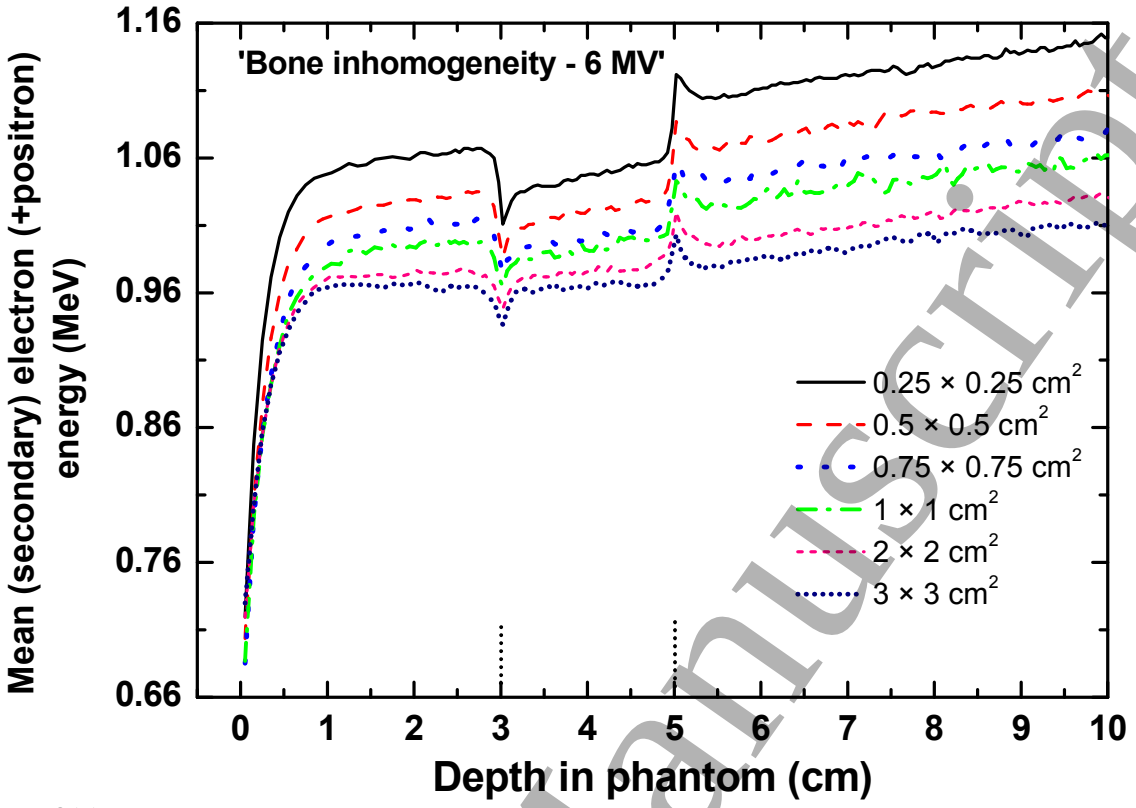

Figure 8(b).

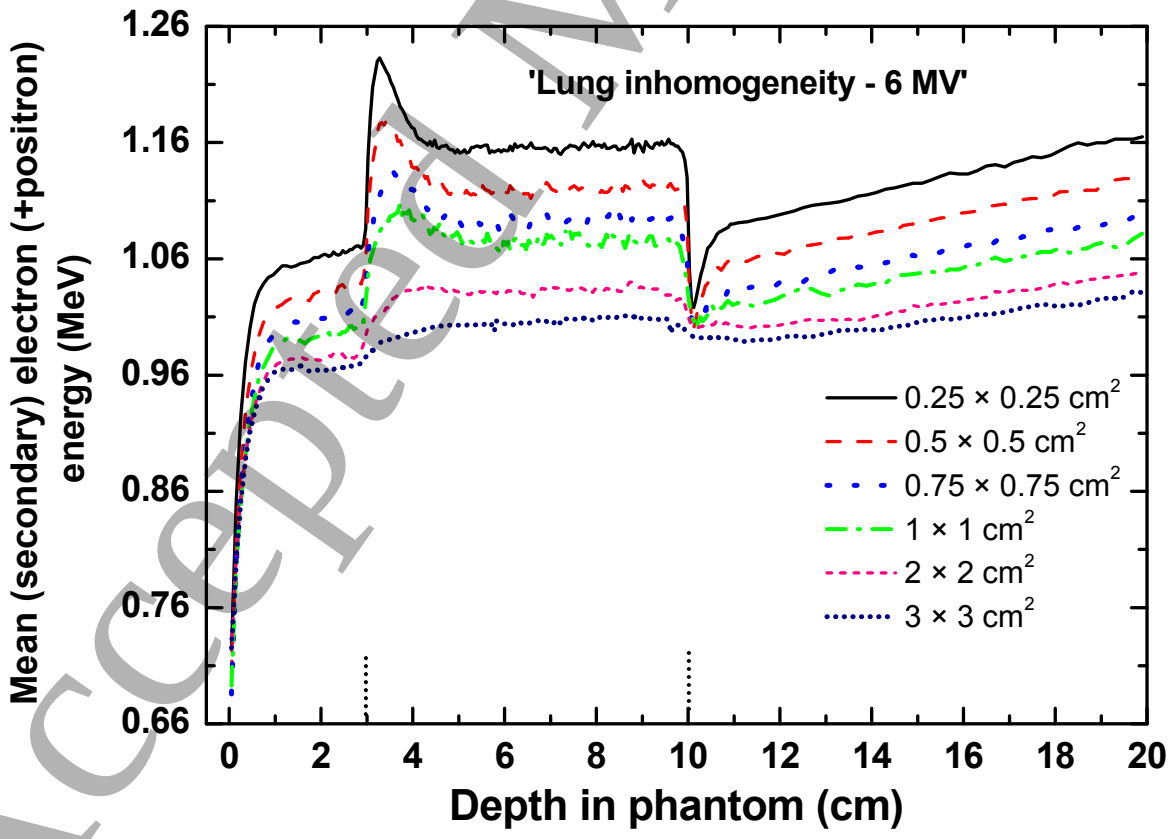

Figure 9.

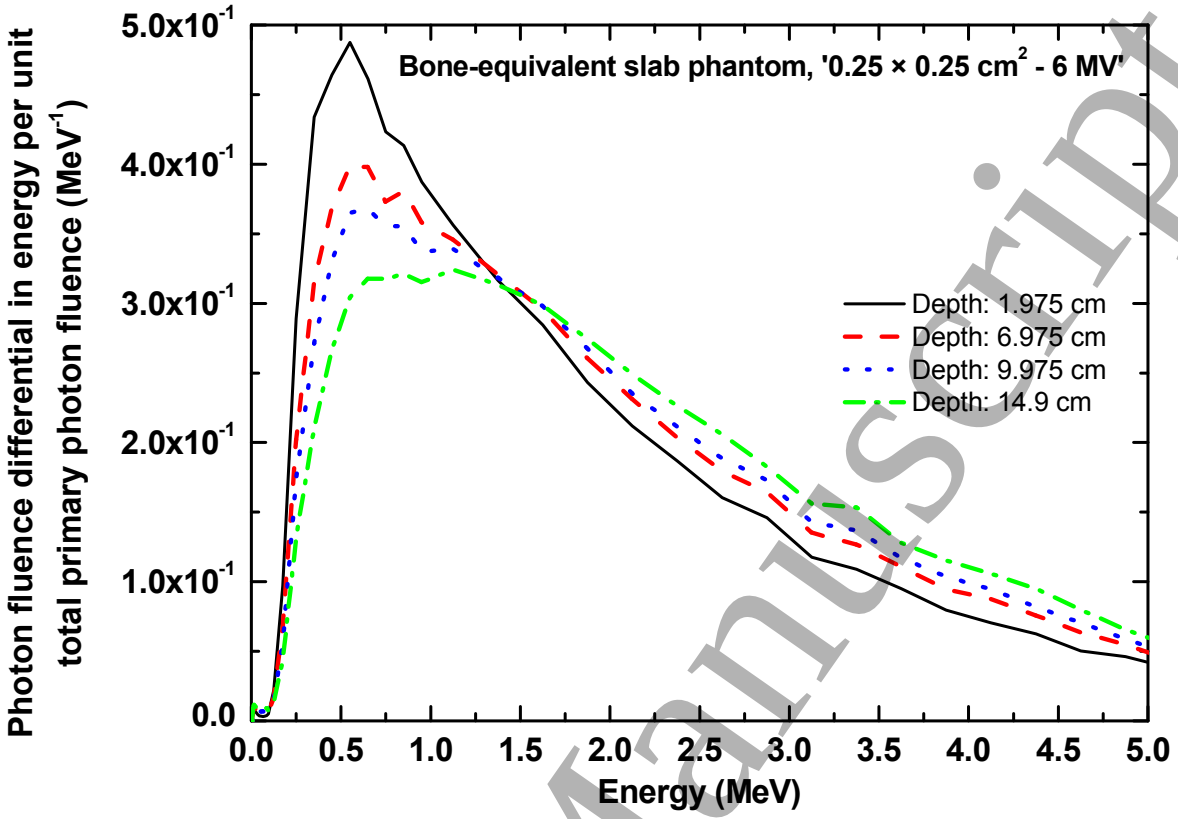

Figure 10(a).

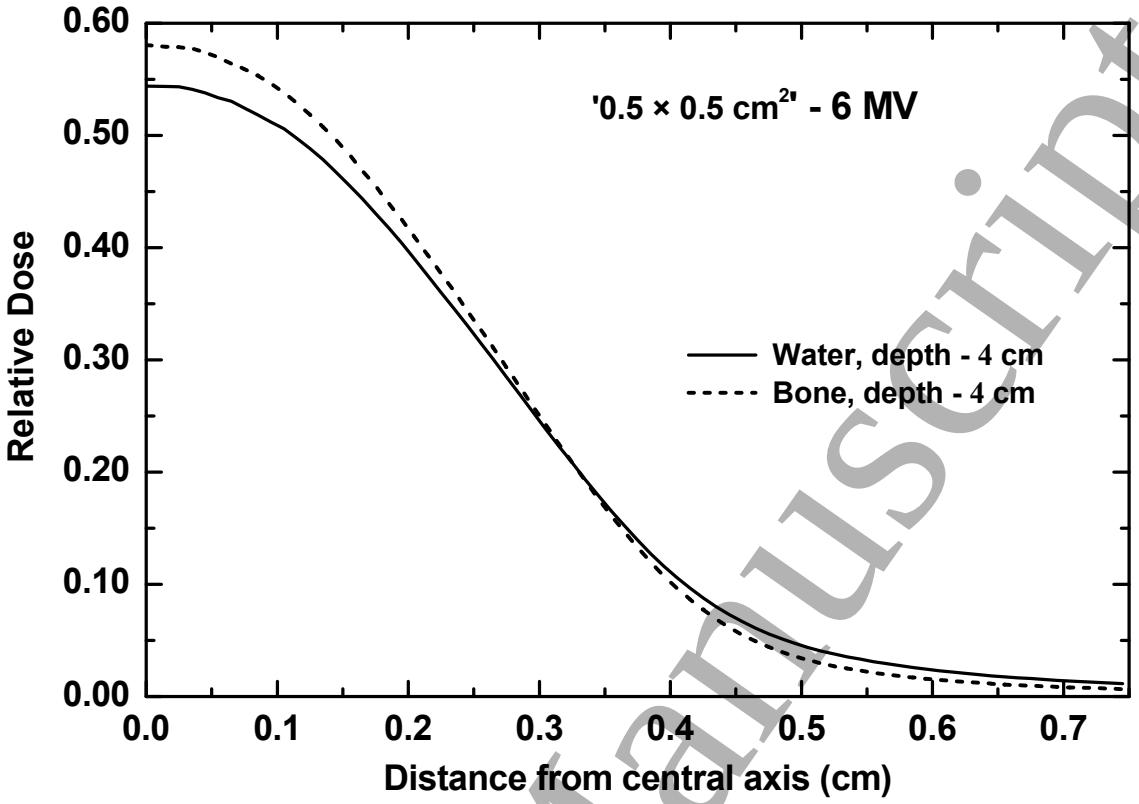

Figure 10(b).

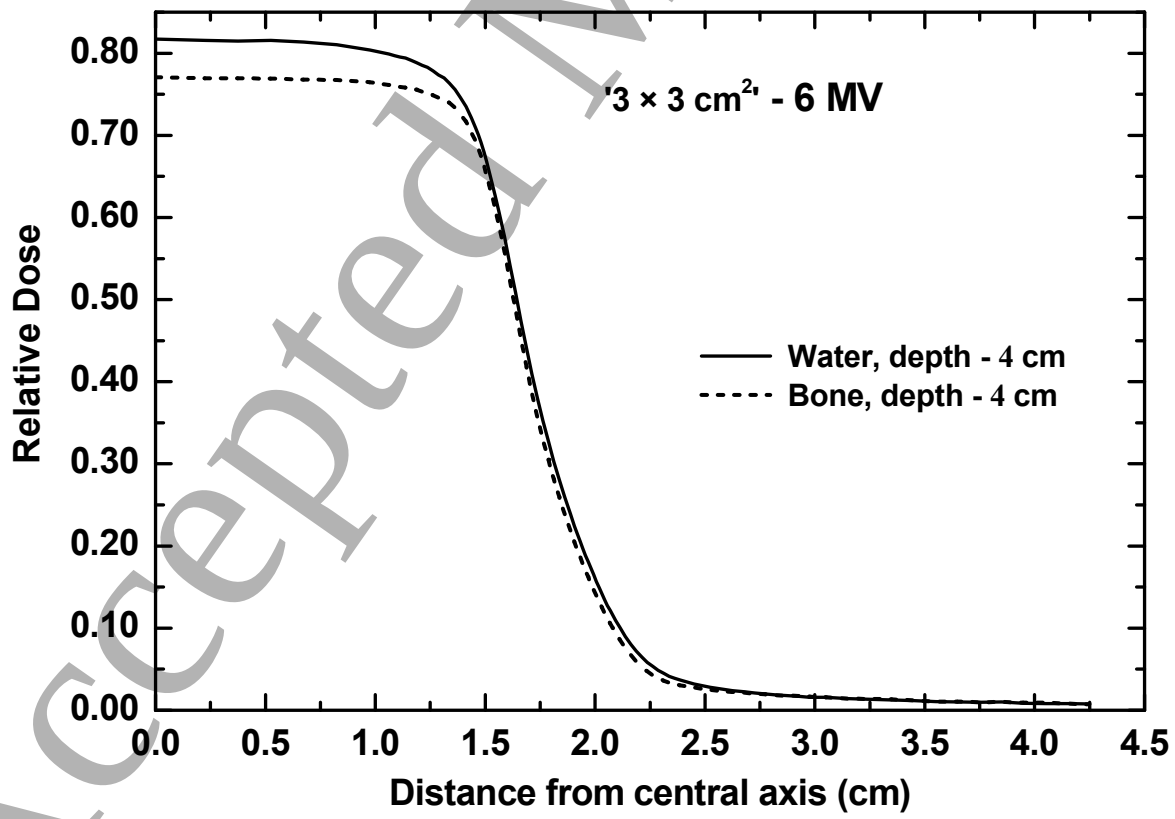

Figure 10(c).

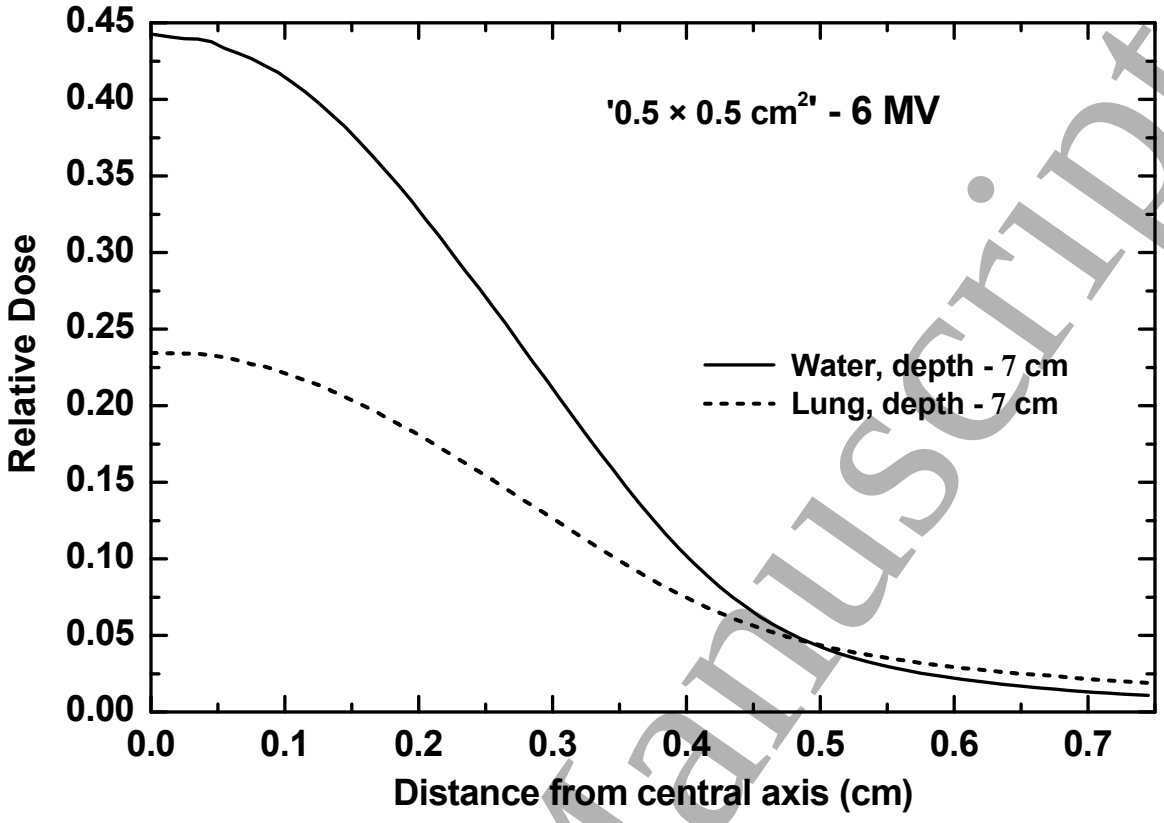

Figure 10(d).

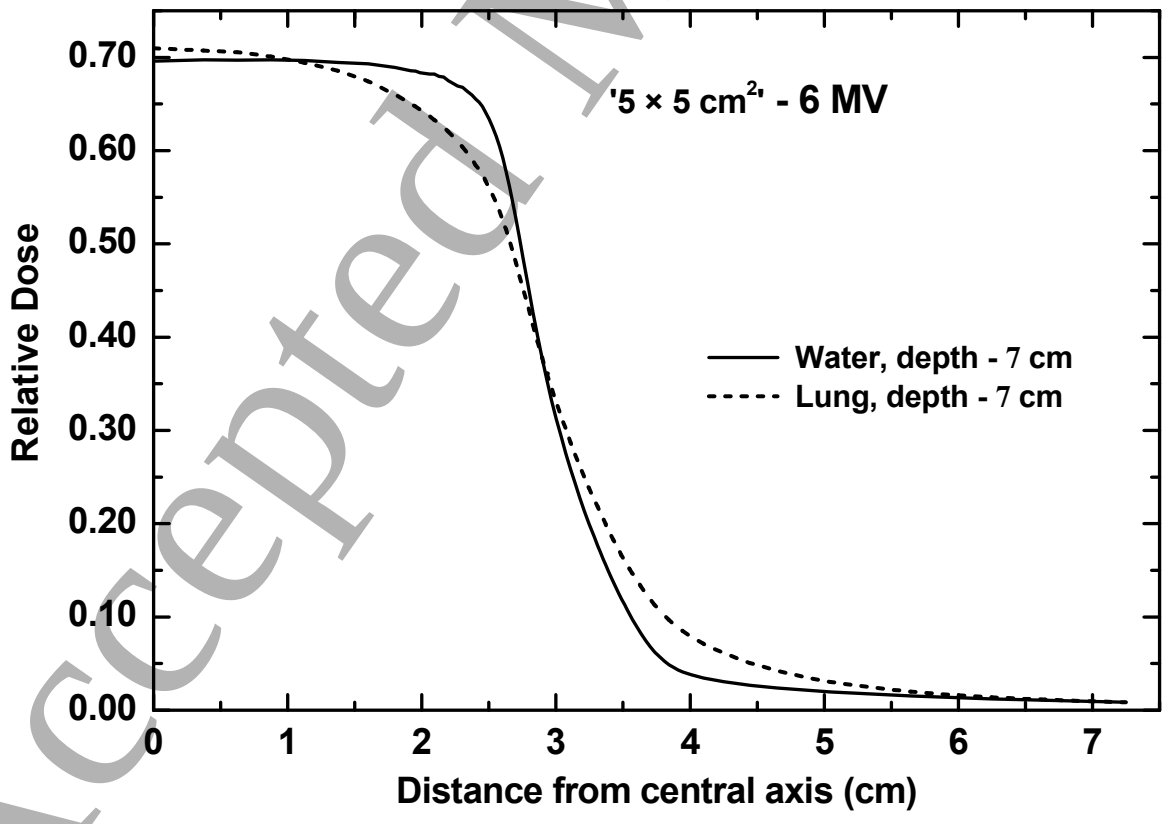

Table 1.

Monte-Carlo transport parameters	Setting
Threshold total energy inelastic collisions (production threshold knock-on electrons)	*AE* = 512 keV
Threshold energy radiative collisions (production threshold for secondary bremsstrahlung photons)	*AP* = 1 keV
Electron/positron total energy cut-off	*ECUT* = 512 keV
Photon energy cut-off	*PCUT* = 1 keV
Bound Compton scattering	On
Rayleigh scattering	On
Atomic relaxations	On
Spin effects	On
Bremsstrahlung cross sections	NIST[7]
Electron impact ionization	On
Photon cross sections	XCOM[8]
Bremsstrahlung angular sampling	KM[9]
Pair angular sampling	KM
Photoelectron angular sampling	On
Boundary crossing algorithm (BCA)	EXACT
Skin depth for BCA	3
Electron-step algorithm	PRESTA-II
ESTEPE	0.25 (default)

[7] Hubbell and Seltzer 2004

[8] Berger *et al* 2010

[9] Koch and Motz

Table 2.

Material simulated	Mass density (g cm^{-3})	Mean excitation energy (eV)	Atomic composition (%)				
			H	C	N	O	Other
Water[10] (ICRU-90, 2016)	0.998	78.0	11.19			88.81	
Lung (inflated)[11] (ICRU-44 1989)	0.21	75.2	10.30	10.50	3.10	74.90	Na 0.2, P 0.2, S 0.3, Cl 0.3, K 0.2
Bone (cortical)[12] (ICRP-23 1975)	1.80	106.4	4.72	14.43	4.20	44.61	Mg 0.22, P 10.5, S 0.315, Ca 20.99, Zn 0.01

[10]Number of electrons per gram = 3.34×10^{23}
[11]Number of electrons per gram = 3.31×10^{23}
[12]Number of electrons per gram = 3.00×10^{23}

Dose, kerma and fluence distributions in heterogeneous slab geometries under non-equilibrium conditions

Table 3.

$$\bar{g} = \left(1 - \left(K_{\mathrm{col}}/K\right)\right)$$

Field Size (cm × cm)	Cortical bone (depth: 3.975 cm)		Inflated lung (depth: 6.475 cm)		Water (depth: 6.475 cm)	
	6 MV	15 MV	6 MV	15 MV	6 MV	15 MV
0.25 × 0.25	$7.940 \times 10^{-3} \pm 0.18\%$	$1.943 \times 10^{-2} \pm 0.12\%$	$4.476 \times 10^{-3} \pm 0.23\%$	$1.190 \times 10^{-2} \pm 0.14\%$	$4.717 \times 10^{-3} \pm 0.22\%$	$1.271 \times 10^{-2} \pm 0.14\%$
0.5 × 0.5	$7.696 \times 10^{-3} \pm 0.17\%$	$1.905 \times 10^{-2} \pm 0.11\%$	$4.372 \times 10^{-3} \pm 0.23\%$	$1.166 \times 10^{-2} \pm 0.13\%$	$4.567 \times 10^{-3} \pm 0.22\%$	$1.239 \times 10^{-2} \pm 0.13\%$
0.75 × 0.75	$7.538 \times 10^{-3} \pm 0.18\%$	$1.900 \times 10^{-2} \pm 0.12\%$	$4.345 \times 10^{-3} \pm 0.22\%$	$1.177 \times 10^{-2} \pm 0.14\%$	$4.502 \times 10^{-3} \pm 0.22\%$	$1.237 \times 10^{-2} \pm 0.14\%$
1 × 1	$7.396 \times 10^{-3} \pm 0.18\%$	$1.850 \times 10^{-2} \pm 0.12\%$	$4.316 \times 10^{-3} \pm 0.24\%$	$1.158 \times 10^{-2} \pm 0.14\%$	$4.434 \times 10^{-3} \pm 0.23\%$	$1.214 \times 10^{-2} \pm 0.14\%$
2 × 2	$6.980 \times 10^{-3} \pm 0.17\%$	$1.772 \times 10^{-2} \pm 0.11\%$	$4.255 \times 10^{-3} \pm 0.23\%$	$1.145 \times 10^{-2} \pm 0.13\%$	$4.184 \times 10^{-3} \pm 0.22\%$	$1.173 \times 10^{-2} \pm 0.13\%$
3 × 3	$6.663 \times 10^{-3} \pm 0.18\%$	$1.697 \times 10^{-2} \pm 0.13\%$	$4.208 \times 10^{-3} \pm 0.23\%$	$1.124 \times 10^{-2} \pm 0.14\%$	$3.968 \times 10^{-3} \pm 0.22\%$	$1.126 \times 10^{-2} \pm 0.14\%$
5 × 5	------	$1.587 \times 10^{-2} \pm 0.11\%$	$4.182 \times 10^{-3} \pm 0.24\%$	--------	$3.840 \times 10^{-3} \pm 0.22\%$	$1.052 \times 10^{-2} \pm 0.14\%$
10 × 10	-------	$1.404 \times 10^{-2} \pm 0.12\%$	--------	$9.964 \times 10^{-3} \pm 0.14\%$	--------	$8.983 \times 10^{-3} \pm 0.14\%$
16 × 16	-------	-------	--------	$9.218 \times 10^{-3} \pm 0.13\%$	--------	$7.869 \times 10^{-3} \pm 0.14\%$

Dose, kerma and fluence distributions in heterogeneous slab geometries under non-equilibrium conditions

Table 4.

Field Size (cm × cm)	Primary electron fluence perturbation correction factors, Bone-to-water, $(p_{\Phi})_{w}^{bone}$ 6 MV	Bone-to-water, $(p_{\Phi})_{w}^{bone}$ 15 MV	Lung-to-water, $(p_{\Phi})_{w}^{lung}$ 6 MV	Lung-to-water, $(p_{\Phi})_{w}^{lung}$ 15 MV
0.25 × 0.25	1.231 ± 0.007	1.403 ± 0.018	0.454 ± 0.003	0.333 ± 0.003
0.5 × 0.5[13]	1.181 ± 0.007	1.355 ± 0.010	0.503 ± 0.004	0.363 ± 0.003
0.75 × 0.75	1.125 ± 0.010	1.308 ± 0.009	0.577 ± 0.006	0.406 ± 0.002
1 × 1	1.087 ± 0.009	1.272 ± 0.007	0.629 ± 0.007	0.434 ± 0.002
2 × 2	1.047 ± 0.006	1.188 ± 0.003	0.811 ± 0.006	0.541 ± 0.002
3 × 3	1.047 ± 0.008	1.138 ± 0.003	0.889 ± 0.005	0.630 ± 0.002
5 × 5	--------	1.093 ± 0.005	1.001 ± 0.007	-------
10 × 10	--------	1.096 ± 0.003	-------	0.945 ± 0.004
16 × 16	--------	----------	-------	1.011 ± 0.003

[13]Everywhere in the tables for 15 MV the 0.5 × 0.5 cm^2 field size was actually equal to 0.45 × 0.45 cm^2.

Dose, kerma and fluence distributions in heterogeneous slab geometries under non-equilibrium conditions

Table 5.

	6 MV		15 MV		6 MV		15 MV	
Field Size (cm × cm)	$\left(s^{BG}_{bone,w}\right)_{Eq.(9)}$	$\left(s^{BG}_{bone,w}\right)_{cav\ th}$ (*ESTAR*)[14]	$\left(s^{BG}_{bone,w}\right)_{Eq.(9)}$	$\left(s^{BG}_{bone,w}\right)_{cav\ th}$ (*ESTAR*)	$\left(s^{BG}_{lung,w}\right)_{Eq.(10)}$	$\left(s^{BG}_{lung,w}\right)_{cav\ th}$ (*ESTAR*)	$\left(s^{BG}_{lung,w}\right)_{Eq.(10)}$	$\left(s^{BG}_{lung,w}\right)_{cav\ th}$ (*ESTAR*)
0.25 × 0.25	0.900 ± 0.011	0.897	0.917 ± 0.030	0.904	1.036 ± 0.018	1.009	0.983 ± 0.022	1.037
0.5 × 0.5	0.901 ± 0.013	0.897	0.913 ± 0.017	0.904	1.030 ± 0.019	1.008	0.990 ± 0.020	1.036
0.75 × 0.75	0.908 ± 0.019	0.897	0.912 ± 0.017	0.903	1.017 ± 0.025	1.007	0.987 ± 0.016	1.035
1 × 1	0.909 ± 0.019	0.897	0.912 ± 0.013	0.903	1.021 ± 0.027	1.007	0.995 ± 0.016	1.035
2 × 2	0.902 ± 0.014	0.897	0.905 ± 0.007	0.902	1.011 ± 0.019	1.006	0.992 ± 0.013	1.034
3 × 3	0.906 ± 0.018	0.898	0.907 ± 0.010	0.902	0.996 ± 0.016	1.005	1.005 ± 0.011	1.033
5 × 5	-------	-------	0.909 ± 0.011	0.902	0.998 ± 0.020	1.005	-------	-------
10 × 10	-------	-------	0.905 ± 0.010	0.902			1.004 ± 0.013	1.030
16 × 16	-------	-------	-------	-------			1.006 ± 0.008	1.029

[14] http://physics.nist.gov/PhysRefData/Star/Text/ESTAR.html

Table 6.

	Bragg-Gray (or unrestricted) stopping-power ratio (10 cm × 10 cm),			
	Bone-to-water		Lung-to-water	
Beam quality	$s^{BG}_{bone,w}$ (Siebers *et al* (2000))	$\left(s^{BG}_{bone,w}\right)_{Eq.(9)}$ (Present work)	$s^{BG}_{lung,w}$ (Siebers *et al* (2000))	$\left(s^{BG}_{lung,w}\right)_{Eq.(10)}$ (Present work)
6 MV	0.896	0.902 ± 0.014	1.001	0.998 ± 0.020
15 MV	0.900	0.905 ± 0.010	1.012	1.004 ± 0.013

Table 7.

	Spectral mean energies (MeV), bone-inhomogeneity: depth = 3.975 cm					
	6 MV			15 MV		
Field Size (cm × cm)	Mean Photon Energy	Mean Electron (+positron) Energy	R_{csda}[15] (cm)	Mean Photon Energy	Mean Electron (+positron) Energy	R_{csda} (cm)
0.25 × 0.25	1.861 ± 0.2%	1.047 ± 0.1%	0.285	4.141 ± 0.5%	2.506 ± 0.3%	0.768
0.5 × 0.5	1.806 ± 0.2%	1.019 ± 0.2%	0.276	4.062 ± 0.5%	2.345 ± 0.2%	0.715
0.75 × 0.75	1.769 ± 0.1%	1.000 ± 0.2%	0.270	4.071 ± 0.6%	2.248 ± 0.2%	0.683
1 × 1	1.736 ± 0.1%	0.992 ± 0.3%	0.267	3.970 ± 0.2%	2.189 ± 0.1%	0.664
2 × 2	1.638 ± 0.1%	0.975 ± 0.2%	0.261	3.831 ± 0.1%	2.089 ± 0.1%	0.631
3 × 3	1.562 ± 0.1%	0.963 ± 0.2%	0.257	3.693 ± 0.1%	2.048 ± 0.1%	0.618
5 × 5	------	-------	-----	3.481 ± 0.1%	2.028 ± 0.1%	0.611
10 × 10				3.127 ± 0.1%	1.981 ± 0.1%	0.596

[15]The R_{csda} was computed from the NIST database (http://physics.nist.gov/PhysRefData/Star/Text/ESTAR.html) by using the mean electron (+positron) energy for each spectrum.

Table 8.

Field Size (cm × cm)	Spectral mean energies (MeV), lung-inhomogeneity: depth = 6.975 cm					
	6 MV			15 MV		
	Mean Photon Energy	Mean Electron (+positron) Energy	*R*csda (cm)	Photon	Electron (+ positron)	Rcsda (cm)
0.25 × 0.25	1.869 ± 0.2%	1.155 ± 0.2%	2.483	4.168 ± 0.5%	2.990 ± 0.3%	7.071
0.5 × 0.5	1.829 ± 0.2%	1.116 ± 0.3%	2.383	4.090 ± 0.6%	2.831 ± 0.3%	6.681
0.75 × 0.75	1.819 ± 0.1%	1.089 ± 0.3%	2.314	4.121 ± 0.3%	2.699 ± 0.2%	6.357
1 × 1	1.808 ± 0.1%	1.068 ± 0.4%	2.261	4.067 ± 0.2%	2.626 ± 0.2%	6.179
2 × 2	1.784 ± 0.1%	1.032 ± 0.2%	2.171	4.034 ± 0.1%	2.449 ± 0.1%	5.744
3 × 3	1.765 ± 0.1%	1.018 ± 0.3%	2.135	3.979 ± 0.1%	2.355 ± 0.1%	5.509
5 × 5	1.755 ± 0.2%	1.004 ± 0.2%	2.100	-------	-------	-------
10 × 10	-------	-------	-----	3.620 ± 0.1%	2.065 ± 0.1%	4.788
16 × 16	-------	-------	-----	3.390 ± 0.1%	2.004 ± 0.1%	4.637